# Electronic structure of NiO: Antiferromagnetic transition and photoelectron spectra in the ordered phase

R. Eder

*Karlsruhe Institute of Technology, Institute for Solid State Physics, 76021 Karlsruhe, Germany*

(Received 26 March 2015; revised manuscript received 29 May 2015; published 19 June 2015)

The thermodynamics of the antiferromagnetic ordering transition in NiO and the photoelectron spectra in the antiferromagnetic phase are studied by the variational cluster approximation. Using realistic Racah parameters to describe the Coulomb interaction in the Ni $3d$ shell and a Slater-Koster parameter $(pd\sigma)$ which is slightly (10%) increased over the band-structure estimate, the calculated Néel temperature is 481 K (experimental value: 523 K). The magnetic susceptibility above $T_N$ has Curie-Weiss form. A significant contribution to the stabilization of the antiferromagnetic phase comes from electron hopping between oxygen which would be missed in theories that consider superexchange along a single bond only. The single-particle spectral function in the ordered phase is in good agreement with experiment, in particular, a number of dispersionless bands which are not reproduced by most calculations are obtained correctly. These flat bands are shown to be direct experimental evidence for a dispersionless electronic self-energy with several poles in the energy range of the valence band which originate from the multiplets of the $Ni^{3+}$ ion. Small but possibly experimentally detectable changes of the photoelectron spectra with temperature are discussed, in particular, a widening of the insulating gap in the paramagnetic phase by approximately 10% is predicted.

DOI: 10.1103/PhysRevB.91.245146 PACS number(s): 74.20.Mn, 74.25.Dw

## I. INTRODUCTION

Nickel oxide has received attention over several decades because it is the prototype of a correlated insulator. As early as 1937, this material was cited as a counterexample to the Bloch theory of solids [1]: assuming strong ionicity, oxygen will be $O^{2-}$ leaving nickel to be $Ni^{2+}$ or [Ar] $3d^8$. This means that four electrons per spin direction have to be distributed over five Ni $3d$ bands which could result in an insulating ground state only if one of the five bands were split off from the others over the entire Brillouin zone. This is impossible, however, because at $\Gamma$ the five Ni $3d$ bands converge into one threefold degenerate $(t_{2g})$ and one twofold degenerate $(e_g)$ level. Band-structure calculations for the paramagnetic phase of NiO [2] confirm this, showing three O $2p$ derived bands well below the Fermi energy and a group of five Ni $3d$ bands which are intersected by the Fermi energy.

This simple picture is modified in that NiO undergoes an antiferromagnetic ordering transition at $T_N = 523$ K. Thereby, Ni ions in planes perpendicular to (1,1,1) align their magnetic moments parallel to each other, with the ordered moment in successive planes being antiparallel (type-II antiferromagnetism). This structure is consistent with the Goodenough-Kanamori rules because all 180° Ni-O-Ni bonds are antiferromagnetic in this way. Band-structure calculations within the framework of density functional theory (DFT) for the antiferromagnetic phase reproduce the insulating ground state, but the band gap is only $G \approx 0.3$ eV [3] whereas the experimental value is $G \approx 4.3$ eV [4]. It should be noted, however, that DFT does indeed give a rather accurate estimate of $G = 4.1$ eV for the single-particle gap in NiO [5] if one does not use the band structure of Kohn-Sham eigenvalues (which have no true physical significance anyway) but calculates the ground-state energy $E_0$ of finite clusters as a function of electron number $N$ and uses $G = E_0(N+1) + E_0(N-1) - 2E_0(N)$. The crucial point is, however, that NiO remains an insulator even above $T_N$ so that the insulating nature of NiO cannot be explained by antiferromagnetic ordering.

There is general agreement by now that the true origin of the insulating nature of NiO is the strong Coulomb interaction between electrons in the Ni $3d$ shell so that an adequate description requires a more accurate treatment of the electron-electron interaction. Accordingly, a wide variety of methods for treating interacting electrons have been applied to NiO over the years. Amongst others there are calculations using the self-interaction corrected density functional theory [6,7], the LDA + $U$ formalism [8,9], and the $GW$ approximation [10,11] which, more recently, was also combined with the LDA + $U$ formalism [12]. NiO was also treated in the framework of the three-body scattering formalism [13,14] and dynamical mean-field theory (DMFT), both for the paramagnetic [15–17] and antiferromagnetic [18] phases. Moreover it was shown recently that within DFT the agreement between calculated and measured band gap for antiferromagnetic NiO is improved considerably by using a screened hybrid density functional [19].

A quite different, but very successful, approach was initiated by Fujimori and Minami [20]. These authors showed that good agreement between theory and experiment could be obtained for angle-integrated valence band photoemission spectra if one focused on local physics by considering an octahedron-shaped $NiO_6^{10-}$ cluster comprising of a single Ni ion and its six nearest-neighbor oxygen ions. The eigenstates and eigenenergies of such a finite cluster can be calculated exactly by the configuration interaction (CI) (or exact diagonalization) method and the single-particle spectral function be obtained from its Lehmann representation. The CI method was subsequently applied to the calculation of the angle-integrated valence band photoemission spectra of a number of transition-metal compounds [21–29] and was extended to simulate x-ray absorption spectra [30–38]. In all cases the agreement with experiment is excellent, and in the case of

 

x-ray absorption spectroscopy, the comparison of simulated and measured spectra by now is in fact becoming a routine tool for determining the valence and spin state of transition-metal ions in solids [39,40].

The reason for the success of the cluster method is that it takes into account the full Coulomb interaction between electrons in the transition-metal $3d$ shell in the framework of atomic multiplet theory [41–43]. Introducing the compound index $\nu = (n,l,m,\sigma)$ (where $n = 3$ and $l = 2$ for a $3d$ shell) the Coulomb interaction between electrons in atomic shells can be written as [41–43]

$$H_1 = \frac{1}{2}\sum_{i,j,k,l} V(\nu_i,\nu_j,\nu_k,\nu_l)\, c^\dagger_{\nu_i} c^\dagger_{\nu_j} c_{\nu_l} c_{\nu_k},$$
$$V(\nu_1,\nu_2,\nu_3,\nu_4) = \delta_{\sigma_1,\sigma_4}\,\delta_{\sigma_2,\sigma_3}\,\delta_{m_1+m_2,m_3+m_4} \times \sum_k F^k\, c^k(l_1 m_1; l_4 m_4)\, c^k(l_3 m_3; l_2 m_2). \tag{1}$$

Here, the $c^k(lm_3;lm_2)$ denote Gaunt coefficients, the $F^k$ Slater integrals, and for a $d$ shell the multipole index $k \in \{0,2,4\}$. The Hamiltonian (1) was derived originally to explain the line spectra of atoms and ions in vacuum (see Ref. [41] for an extensive list of examples). There are various simplified expressions in the literature [44] where the Hamiltonian (1) is approximated in terms of Hubbard $U$ and Hund's rule $J$ and sometimes additional parameters (see Ref. [45] for the relation between Hubbard $U$ and Hund's rule $J$ and the Slater integrals), but the Hamiltonian (1) is the only one that can actually be derived from first principles and gives correct results for free ions [an instructive comparison of the eigenvalue spectra of the original Hamiltonian (1) and various simplified versions was given by Haverkort [46]]. $H_1$ contains diagonal terms such as

$$[V(\nu_1,\nu_2,\nu_1,\nu_2) - V(\nu_1,\nu_2,\nu_2,\nu_1)] n_{\nu_1} n_{\nu_2} \tag{2}$$

but also off-diagonal terms where all four $\nu_i$ in Eq. (1) are pairwise different. The off-diagonal matrix elements are frequently discarded in DMFT calculations [15,16] because they exchange electrons and thus exacerbate the minus-sign problem in quantum Monte Carlo calculations (more recently it has become possible to include off-diagonal terms by using the continuous time Monte Carlo algorithm [47]). On the other hand, the matrix elements of these terms are of the same order of magnitude (namely proportional to the Slater integrals $F^2$ and $F^4$) as the differences between the various diagonal matrix elements in Eq. (2) so that there is no justification for discarding them but keeping different diagonal matrix elements.

As will be seen in the following, the variational cluster approximation (VCA) proposed by Potthoff [48–50] allows to extend the scope of the CI method of Fujimori and Minami once more, to the calculation of thermodynamical quantities and band structures for strongly correlated electron systems. Since the VCA is based on exact diagonalization and therefore free from the minus-sign problem, the full Coulomb Hamiltonian (1) including the off-diagonal matrix elements can be included. As could have been expected on the basis of the considerable success of the CI method in reproducing experimental spectra [20–38], the VCA achieves good agreement with experiment.

## II. HAMILTONIAN AND METHOD OF CALCULATION

The method of calculation has been described in detail in Ref. [51], so we give only a brief description. The Hamiltonian describing the NiO lattice is

$$H = H_0 + H_1,$$
$$H_0 = \sum_{i\alpha\sigma} \epsilon_\alpha\, d^\dagger_{i\alpha\sigma} d_{i\alpha\sigma} + H_{pd} + H_{pp} + H_{dd}, \tag{3}$$
$$H_{pd} = \sum_{i\alpha,j\beta}\sum_\sigma (t_{i\alpha,j\beta}\, d^\dagger_{i\alpha\sigma}\, p_{j\beta\sigma} + \text{H.c.}),$$

where, e.g., $d^\dagger_{i\alpha\sigma}$ creates an electron with $z$ spin $\sigma$ in the Ni $3d$ orbital $\alpha \in \{xy,xz,\ldots,3z^2-r^2\}$ at the Ni site $i$ whereas $p^\dagger_{j\beta\sigma}$ creates an electron in the O $2p$ orbital $\beta \in \{x,y,z\}$ at the O site $j$. The energy of the O $2p$ orbitals is the zero of energy. The terms $H_{pp}$ and $H_{dd}$ describe hopping between two O $2p$ orbitals or two Ni $3d$ orbitals, respectively, and their form is self-evident. The parameters in this Hamiltonian have been obtained from a fit to an LDA band structure and are listed in Table I of Ref. [51]. One noteworthy detail is that the energies $\epsilon_\alpha$ have to be subject to the "double-counting correction": $\epsilon_\alpha \to \epsilon_\alpha - nU$ with $U$ the Hubbard $U$ (see Ref. [51] for a detailed discussion). The interaction Hamiltonian $H_1$ has the form (1) for each Ni $3d$ shell, the Racah parameters were $A = 7\,\text{eV}$, $B = 0.13\,\text{eV}$, $C = 0.6\,\text{eV}$, resulting in the Slater integrals $F^0 = 7.84\,\text{eV}$, $F^2 = 10.57\,\text{eV}$, and $F^4 = 7.56\,\text{eV}$. The dependence of the Slater integrals on the $d$-shell occupation and also on the crystal-field level was neglected. An important detail is that there is a nonvanishing interaction only between Ni $3d$ orbitals in the same Ni ion.

For a multiband system such as (3) the imaginary-time Green's function $\mathbf{G}(\mathbf{k},i\omega_\nu)$ and self-energy $\Sigma(\mathbf{k},i\omega_\nu)$ are matrices of dimension $2n_{\text{orb}} \times 2n_{\text{orb}}$ with $n_{\text{orb}}$ the number of orbitals/unit cell. In the following, we will often omit the $\mathbf{k},i\omega_\nu$ argument on these quantities for brevity.

The starting point for the VCA is an expression for the grand canonical potential of an interacting Fermi system derived by Luttinger and Ward [52]:

$$\Omega = -\frac{1}{\beta}\sum_{\mathbf{k},\nu} e^{i\omega_\nu 0^+}[\ln\det(-\mathbf{G}^{-1}) + \text{tr}\,\Sigma\mathbf{G}] + \Phi[\mathbf{G}]. \tag{4}$$

Here, $\Phi[\mathbf{G}]$ denotes the so-called Luttinger-Ward functional which was defined originally [52] as a sum over infinitely many closed, connected, skeleton diagrams with the noninteracting Green's function $\mathbf{G}_0$ replaced by the argument of the functional $\mathbf{G}$. A nonperturbative construction of $\Phi[\mathbf{G}]$ has been given by Potthoff [53,54]. In their proof of (4), Luttinger and Ward derived two important results: first, $\Phi[\mathbf{G}]$ is the generating functional of the self-energy

$$\frac{\partial\Phi[\mathbf{G}]}{\partial G_{\alpha\beta}(\mathbf{k},i\omega_\nu)} = \frac{1}{\beta}\,\Sigma_{\beta\alpha}(\mathbf{k},i\omega_\nu) \tag{5}$$

and, second, $\Omega$ is stationary under variations of $\Sigma$

$$\frac{\partial\Omega}{\partial\Sigma_{\alpha\beta}(\mathbf{k},i\omega_\nu)} = 0. \tag{6}$$

The first of these equations can be used [48,49] to define the Legendre transform $F[\mathbf{\Sigma}]$ of $\Phi[\mathbf{G}]$ via

$$F[\Sigma] = \Phi[\mathbf{G}[\Sigma]] - \frac{1}{\beta}\sum_{\mathbf{k},\nu} \mathrm{tr}\,\Sigma\,\mathbf{G}.$$

Introducing the noninteracting Green's function $\mathbf{G}_0$, $\Omega$ thus can be expressed as a functional of $\Sigma$:

$$\Omega = -\frac{1}{\beta}\sum_{\mathbf{k},\nu} e^{i\omega_\nu 0^+}\left[\ln\det\left(-\mathbf{G}_0^{-1}+\Sigma\right)\right] + F[\Sigma] \qquad (7)$$

which is known to be stationary at the exact $\Sigma(\omega)$ by virtue of (6). The problem one faces in the practical application of this stationarity principle is that no explicit functional form of $F[\Sigma]$ is known.

In the framework of the VCA this problem is circumvented as follows [48–50]: first, we note that $\Phi[\mathbf{G}]$ involves only the interaction part $H_1$ of the Hamiltonian (via the interaction lines in the skeleton diagrams) and the Green's function $\mathbf{G}$ (via the Green's function lines); the latter, however, is the argument of the functional. This implies that the functional $\Phi[\mathbf{G}]$ and its Legendre transform $F[\Sigma]$ are the same for any two systems with the same interaction part $H_1$ (Potthoff has derived this property without making any reference to diagrams [53,54]). In the application to NiO we accordingly consider two systems: system I is the original NiO lattice described by the Hamiltonian (3) whereas system II, termed the reference system by Potthoff [48–50], is an array of clusters, each of which consists of the five Ni $3d$ orbitals of one Ni ion of the original NiO lattice plus five ligands or bath sites [48,49] which hybridize with these. The single-particle Hamiltonian of such a cluster is

$$\tilde{H}_0 = \sum_{\alpha,\sigma}[\epsilon_d(\alpha)\,d^\dagger_{\alpha,\sigma}d_{\alpha,\sigma} + \epsilon_L(\alpha)\,l^\dagger_{\alpha,\sigma}l_{\alpha,\sigma}] + \sum_{\alpha,\sigma}[V(\alpha)\,d^\dagger_{\alpha,\sigma}l_{\alpha,\sigma} + \mathrm{H.c.}], \qquad (8)$$

where $\alpha \in \{xy, xz \ldots 3z^2 - r^2\}$ whereas the interaction part $H_1$ for each cluster is again given by (1). In the CI method by Fujimori and Minami the ligand $l_\alpha$ would be the linear combination of O $2p$ orbitals on the six oxygen ions surrounding the Ni ion under consideration which hybridizes with the $d$ orbital $d_\alpha$. In the case of the VCA, the ligands are purely mathematical objects which have no counterpart in the physical system and which are introduced solely for the purpose of constructing self-energies. Accordingly, there are *no* terms coupling the clusters centered on neighboring Ni ions in system II which therefore consists of completely disconnected finite clusters. The crucial point is that since the interaction parts of systems I and II are identical by construction, they have the same Luttinger-Ward functional $F[\Sigma]$. Since the individual clusters of system II are relatively small (they comprise 10 orbitals/spin direction), they can be treated by exact diagonalization and we can obtain all eigenstates of $H - \mu N$ within $\approx 20 k_B T$ above the minimum value. Using these the grand potential $\tilde{\Omega}$ can be evaluated numerically (quantities with a tilde refer to a cluster in the following) and the full Green's function $\tilde{\mathbf{G}}(\omega)$ be calculated (e.g., by using the Lanczos algorithm). Next, $\tilde{\mathbf{G}}(\omega)$ can be inverted numerically for each $\omega$ and the self-energy $\tilde{\Sigma}(\omega)$ be extracted. Thereby we have in real-space representation $\tilde{\Sigma}_{\alpha\beta}(i,j,\omega) = \tilde{\Sigma}_{\alpha\beta}(\omega)\,\delta_{ij}$ where $i,j$ are the indices of the individual disconnected clusters and moreover $\tilde{\Sigma}_{\alpha\beta}(\omega) \neq 0$ only if both indices $\alpha$ and $\beta$ refer to Ni $3d$ orbitals. The resulting self-energy thus is $\mathbf{k}$ independent and bears no more reference to the fictitious ligands.

Using $\tilde{\Omega}$ and $\tilde{\Sigma}(\omega)$, Eq. (7), now applied to a single cluster, can be reverted to obtain the numerical value of $F[\tilde{\Sigma}]$ for the self-energy $\tilde{\Sigma}(\omega)$. By taking the digression to the reference system of clusters it is thus possible to generate self-energies for which the exact numerical value of the Luttinger-Ward functional is known. Next, these self-energies are used as "trial self-energies" for the lattice, i.e., we approximate

$$\Omega \approx -\frac{1}{\beta}\sum_{\mathbf{k},\nu} e^{i\omega_\nu 0^+}\left[\ln\det\left(-\mathbf{G}_0^{-1}+\tilde{\Sigma}\right)\right] + N F[\tilde{\Sigma}], \qquad (9)$$

where $\mathbf{G}_0$ now is the noninteracting Green's function of the physical NiO lattice and $N$ the number of Ni sites in this.

The variation of $\tilde{\Sigma}$ is performed by varying the single-particle parameters $\lambda_i$ of the cluster single-particle Hamiltonian (8), that means $\epsilon_d(\alpha)$, $\epsilon_L(\alpha)$, and $V(\alpha)$. These parameters are not determined as yet because the only requirement for the equality of the Luttinger-Ward functionals of the two systems was that the *interaction parts* $H_1$ be identical. In this way, the approximate $\Omega$ (9) becomes a function of the $\lambda_i$, $\Omega = \Omega(\lambda_1, \ldots \lambda_n)$ and the stationarity condition (6) is replaced by a condition on the $\lambda_i$:

$$\frac{\partial\Omega}{\partial\lambda_i} = 0. \qquad (10)$$

The physical interpretation would be that the VCA amounts to seeking the best approximation to the true self-energy of the NiO lattice amongst the "cluster representable" ones. Since its invention by Potthoff, the VCA has been applied to study the Hubbard model in various dimensions [55–65] models for $3d$ transition-metal compounds [66–70] and interacting bosons [71,72]. As discussed by Potthoff [54], the VCA also has some relation to DMFT in that the DMFT self-consistency equation can be derived as one possible solution to the stationarity condition (10) for a continuum of ligands. In contrast to this, (10) can be solved for a finite number of ligands and in fact a rather small number of ligands appears sufficient to obtain reliable results. For example, by using the VCA with a reference system consisting of a single correlated site and one ligand, i.e., a simple dimer, Potthoff could reproduce results for the metal-insulator transition in $d = \infty$ which had been obtained previously with considerably more involved calculations in the framework of DMFT [49].

For the present application to NiO and in the paramagnetic case cubic symmetry reduces the number of parameters $\lambda_i$ to be varied to only six: for each $\alpha$, the Hamiltonian (8) contains three parameters and there is one such set for the $e_g$ orbitals and one for the $t_{2g}$ orbitals. The equation system (10) is solved by the Newton method (see Refs. [51,69] for details). The proposal of Balzer and Potthoff [60] to use rotated and rescaled coordinate axis for the calculation of the derivatives of $\Omega$ with respect to the $\lambda_i$ turned out to be of crucial importance for successful Newton iterations.

The paramagnetic phase of NiO was studied in some detail in the preceding paper [51]. There are only a few differences as compared to this study: first, a reduced value of the Racah parameter $A = 7.0\,\text{eV}$ ($A = 8.25\,\text{eV}$ in Ref. [51]) and consequently a readjustment of the Ni $3d$ orbital energy to $\epsilon_d = -52\,\text{eV}$ (whereas $\epsilon_d = -62\,\text{eV}$ in Ref. [51]). This was done to reduce the spectral weight of the satellite which appeared to be somewhat too high in Ref. [51] while at the same time maintaining the position of the satellite and the insulating gap. The value $A = 7.0\,\text{eV}$ still is well within the range of estimates in the literature (see the discussion in Ref. [51]). Second, the Ni $3d$ to O $2p$ hopping parameter $(pd\sigma)$ was increased by 10% to $-1.4178\,\text{eV}$ (all other LCAO parameters were left unchanged) to bring the calculated Néel temperature closer to the experimental value (see following). Due to improved computer power it was now moreover possible to optimize all relevant single-particle parameters of the octahedral cluster. Thereby it turned out that $V(t_{2g}) = 0$ is a stationary point irrespective of the values of the other parameters. The energy of the $t_{2g}$-like ligand $\epsilon_L(t_{2g})$ then is irrelevant so that only the four parameters $\epsilon_d(e_g)$, $\epsilon_L(e_g)$, $V(e_g)$, and $\epsilon_d(t_{2g})$ remain to be solved for. The resulting paramagnetic solution, however, is stationary with respect to all six possible parameters. Some results for the paramagnetic phase will be presented later in comparison to the antiferromagnetic one.

## III. MAGNETIC SUSCEPTIBILITIES AND ANTIFERROMAGNETIC TRANSITION

We discuss the staggered and uniform magnetic susceptibility. Within the VCA, the grand canonical potential may be thought of as being expressed as a function of a number of parameters

$$\Omega = \Omega(\zeta_1, \ldots \zeta_m, \lambda_1, \ldots, \lambda_n), \tag{11}$$

where the $\zeta_i$ are the parameters of the physical lattice system (such as the physical hopping integrals and orbital energies or certain external fields) and the $\lambda_i$ are the single-electron parameters of the reference system which parametrize the self-energy. We assume that amongst the $\zeta_i$ there is also a uniform or staggered magnetic field $h$ along the $z$ direction. This implies that the values of all single-particle parameters of the reference system must be taken as spin dependent:

$$\lambda_{i,\sigma} = \lambda_{i,+} + \text{sign}(\sigma)\lambda_{i,-},$$

which results in a spin-dependent self-energy $\Sigma_\uparrow(\omega) \neq \Sigma_\downarrow(\omega)$. For a staggered field, we switch to the antiferromagnetic unit cell and assume that the $\lambda_{i,-}$ have opposite sign at the two Ni ions in this cell. This means that the self-energy for an $\uparrow$ electron is $\Sigma_\uparrow(\omega)$ at the first Ni ion and $\Sigma_\downarrow(\omega)$ at the second Ni ion in the antiferromagnetic cell and vice versa for a $\downarrow$ electron ($\mathbf{k}$ sums now have to be performed over the antiferromagnetic Brillouin zone). For a uniform field, we retain the original unit cell and use the spin-dependent self-energy at the single Ni ion in this cell.

We assume that we have found a stationary point $\lambda_i^*$ for $h = 0$, i.e.,

$$\left.\frac{\partial\Omega}{\partial\lambda_i}\right|_{\lambda_i^*} = 0 \tag{12}$$

for all $i$ and denote the grand potential for this solution by $\Omega_0$. Since this is the paramagnetic stationary point, all spin-odd parameters $\lambda_{i,-}$ are zero. Upon applying a small finite $h$ *in the lattice system*, $\Omega$ therefore can be expanded as

$$\Omega = \Omega_0 + \frac{1}{2}\sum_{i,j}\tilde{\lambda}_i\, A_{i,j}\,\tilde{\lambda}_j + \sum_i \tilde{\lambda}_i\, B_i\, h + \frac{1}{2}\, C\, h^2, \tag{13}$$

where the shifts $\tilde{\lambda}_i = \lambda_i - \lambda_i^*$ and $A$, $B$, and $C$ are second derivatives of $\Omega$ at the point $\lambda_i = \lambda_i^*, h = 0$. There are no terms linear in the $\tilde{\lambda}_i$ because of (12) and there is no term linear in $h$ because $\Omega$ must be an even function of $h$. The second derivatives can be evaluated numerically whereby the fact that the $\lambda_i$ are parameters of the reference system whereas the staggered field $h$ is one of the $\zeta_i$ in Eq. (11) causes no problem. Moreover, all derivatives are to be evaluated in the paramagnetic phase, so no calculation in a finite field is necessary. Demanding stationarity, we obtain for the shifts $\tilde{\lambda}_i$

$$\frac{\partial\Omega}{\partial\tilde{\lambda}_i} = \sum_j A_{i,j}\tilde{\lambda}_j + B_i h = 0, \tag{14}$$

and reinserting into (13) we obtain $\Omega$ as a function of $h$ [69]:

$$\Omega(h) = \Omega_0 - \frac{h^2}{2}\,\chi, \quad \chi = \sum_{i,j} B_i A_{i,j}^{-1} B_j - C. \tag{15}$$

$\Omega$ must be invariant under a simultaneous sign change of $h$ and all spin-odd parameters $\bar{\lambda}_{i,-}$ so that $\tilde{\lambda}_{i,+} = 0$ for all $i$ and the sums over $i$ and $j$ in Eq. (15) extend only over the spin-odd parameters.

Figure 1 shows the staggered and uniform susceptibilities obtained in this way as a function of temperature. Thereby the

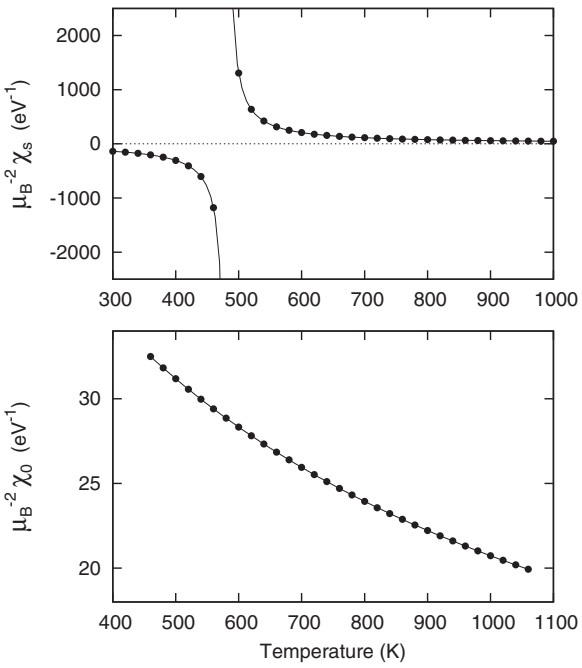


FIG. 1. Staggered (top) and uniform (bottom) susceptibility of NiO. The symbols give the calculated values, the lines are the expressions (16) and (17).

term

$$H_m = -h \sum_i e^{i\mathbf{Q}\cdot\mathbf{R}_i} (n_{i\uparrow} - n_{i\downarrow})$$

was added to the lattice Hamiltonian, so that the physical susceptibilities are given by

$$\chi_{\mathbf{Q}} = -\mu_B^2 \frac{\partial^2 \Omega}{\partial h^2}.$$

The staggered susceptibility can be fitted accurately by

$$\chi_s(T) = \frac{\mu_B^2 C_s}{T - T_N} \tag{16}$$

with $T_N = 481.03\,\mathrm{K}$ and $C_s = 24805\,\mathrm{K\,eV^{-1}}$ whereas the uniform susceptibility can be fitted by

$$\chi_0(T) = \frac{\mu_B^2 C_0}{T + \Theta_{\mathrm{CW}}} \tag{17}$$

with $\Theta_{\mathrm{CW}} = 491.62\,\mathrm{K}$ and $C_0 = 30923\,\mathrm{K\,eV^{-1}}$. The divergence of $\chi_s(T)$ at $T_N$ is due to an eigenvalue of the Hessian $A$ crossing zero at $T_N$.

Interestingly, the Curie-Weiss temperature $\Theta_{\mathrm{CW}}$ is somewhat higher than the Néel temperature $T_N$. This can be understood as a consequence of the type-II antiferromagnetic structure and (weak) antiferromagnetic exchange between Ni ions connected by a 90° Ni-O-Ni bond [an example would be two Ni ions at distance $(a,a,0)$]. For such a pair of Ni ions there is a competition between the direct antiferromagnetic exchange [mediated by the direct Ni-Ni hopping as described by Slater-Koster parameters such as $(dd\sigma)$] and the ferromagnetic exchange due to Hund's rule coupling on oxygen. Let us assume that the net exchange constant between such a pair of Ni ions is antiferromagnetic (this is certainly true for the present calculation which does not include Hund's rule exchange on oxygen). Then, any given Ni ion has 12 neighbors of that type and in the type-II antiferromagnetic structure, the ordered moment of one half of these neighbors is parallel to the moment of the ion at the center whereas it is antiparallel for the other half. The exchange fields due to these 12 neighbors therefore cancel and the Néel temperature is determined solely by the antiferromagnetic superexchange with the six neighbors connected by 180° Ni-O-Ni bonds. On the other hand, the parameter $\Theta_{\mathrm{CW}}$ is a measure as to how strongly the antiferromagnetic exchange between spins opposes a uniform ferromagnetic polarization. For the case of a uniform ferromagnetic polarization, however, the exchange fields from all 12 $(a,a,0)$-like neighbors are parallel and therefore do contribute to $\Theta_{\mathrm{CW}}$. The discrepancy between $T_N$ and $\Theta$ obtained in the VCA calculation thus is to be expected. The experimental value $\Theta_{\mathrm{expt}} = 2000$ K was given in Ref. [73], but being almost four times the experimental Néel temperature this appears somewhat high.

For a Heisenberg antiferromagnet, the constant $C$ would be given by

$$C = \frac{S(S+1)}{3k_B}(g S_{\mathrm{eff}})^2.$$

Using the values from the fits in Fig. 1 with $S = 1$ we obtain the reasonable values $S_{\mathrm{eff}} = 1.000$ for $\chi_0$ and $S_{\mathrm{eff}} = 0.895$ from $\chi_s$. The smaller value for $S_{\mathrm{eff}}$ in the staggered case likely is due to the fact that in the computation of $\chi_0$ the magnetic field is applied to all orbitals in the unit cell, whereas it acts only on the Ni $3d$ orbitals in the case of $\chi_s$.

As might have been expected on the basis of the theory of superexchange, the Néel temperature is quite sensitive to the Slater-Koster parameter $(pd\sigma)$. With the original value $(pd\sigma) - 1.4178\,\mathrm{eV}$ obtained from the fit to the LDA band structure [51] one obtains $T_N = 370\,\mathrm{K}$.

Lastly, we point out an interesting feature of these results: the matrix $A$ of second derivatives of $\Omega$ with respect to the spin-odd parameters $\lambda_{i,-}$ in Eq. (15) obviously is the same in the case of staggered and uniform susceptibility. Only the quantities $B$ and $C$ are different. Still, the resulting susceptibilities have a completely different but physically reasonable temperature dependence.

## IV. ANTIFERROMAGNETIC PHASE

To obtain the results presented so far, only the paramagnetic solution was needed. If we want to discuss the antiferromagnetic phase itself, we need to find stationary points with spin-dependent parameters $\lambda_i$ and this doubling of the number of parameters complicates the numerical problem of finding the stationary point. We recall that in the parmagnetic case a total of four parameters were varied: $\epsilon_d(e_g)$, $\epsilon_L(e_g)$, $V(e_g)$, and $\epsilon_d(t_{2g})$ [moreover, $V(t_{2g}) = 0$ always was a stationary point and with that value the last parameter $\epsilon_L(t_{2g})$ is irrelevant]. Doubling all of the nonvanishing parameters would result in a total of eight parameters. Using the Newton method, this is still numerically manageable but it turned out that a more severe problem appears. While it might seem that the more parameters $\lambda_i$ one is varying, the better an approximation for the self-energy results, calculations showed that the opposite is true. Introducing too many symmetry-breaking parameters $\lambda_{i,-}$ leads to unphysical solutions (one example is discussed in detail in the Appendix). In fact, it turned out that retaining more than two, out of the four possible, $\lambda_{i,-}$ leads to unphysical solutions. Accordingly, in the following we present solutions obtained with six parameters $\lambda_i$. In choosing the $\lambda_{i,-}$ to be kept we heuristically use the staggered susceptibility $\chi_s$ as a guidance. Namely, we can restrict the set of the $\lambda_{i,-}$ in the expression (15) for $\chi_s$ to only 2 and examine which combination still gives a $\chi_s$ which is closest to the one obtained with the full set of 4 $\lambda_{i,-}$. It turned out that retaining only the spin-odd part of the $e_g$-like hopping integral $V_-(e_g)$ and the $t_{2g}$-like $d$-level energy $\epsilon_{d,-}(t_{2g})$ the staggered susceptibility $\chi_s$, and in particular the Néel temperature, remain practically unchanged. This appears plausible because the physical mechanism that stabilizes antiferromagnetism in NiO is the enhanced hopping for the $e_g$ electrons of one spin direction along the 180° Ni-O-Ni bonds connecting sites on different sublattices. A spin-dependent $d$-level-to-ligand hopping then clearly is the best way to simulate this effect in a cluster with only a single Ni ion. Since we have set $V(t_{2g}) = 0$ in the paramagnetic case, $\epsilon_d(t_{2g})$ moreover is the only remaining parameter pertinent to the $t_{2g}$ orbitals. In the following, the resulting solution will be referred to as AF-I.

In addition, there is a second type of antiferromagnetic solution where $V_+(e_g) = V_-(e_g)$ so that the hopping for one

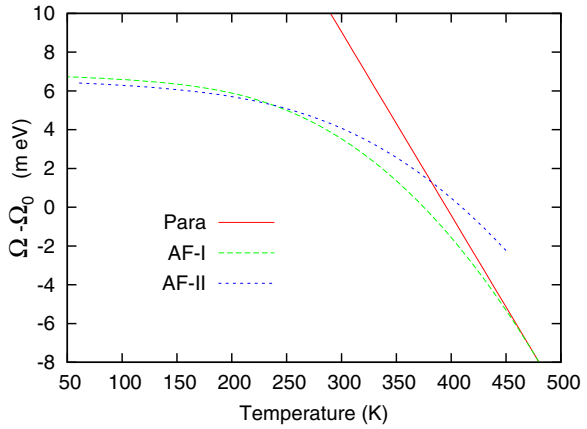


FIG. 2. (Color online) Grand potential per Ni ion for the various solutions described in the text as a function of temperature. $\Omega_0 = -356.042\,\text{eV}$ is an arbitrary reference energy.

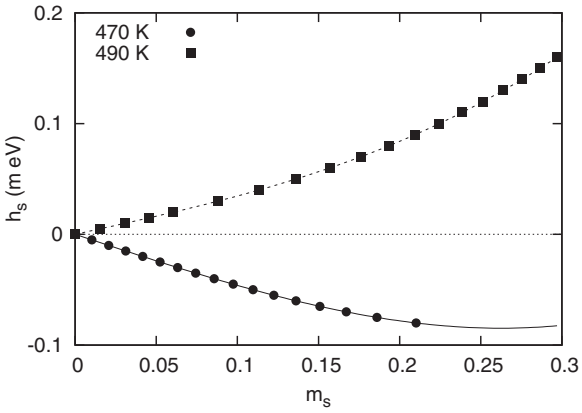


FIG. 3. Staggered field versus staggered magnetization below and above $T_N$. The lines are the cubic fits discussed in the text.

spin direction of $e_g$ electrons is exactly zero. In this case, the only remaining spin-odd parameters to be varied are $\epsilon_{d,-}(t_{2g})$ and $\epsilon_{d,-}(e_g)$ [since one spin direction of the $e_g$ electrons has zero hopping, the spin splitting of the $e_g$-like ligand $\epsilon_{L,-}(e_g)$ is irrelevant and can be set to zero]. It should be stressed that in this case $\Omega$ is stationary also with respect to $V_-(e_g)$, and the values $V_+(t_{2g}) = V_-(t_{2g}) = 0$ remain stationary as in the paramagnetic case. Despite the fact that only 6 parameters are actually varied, the corresponding solution therefore is stationary with respect to all 12 possible parameters of the cluster. This solution will be referred to as AF-II. Lastly, it should be emphasized that the magnetic order described by both solutions is type-II antiferromagnetism. The solutions differ by the parameters of the reference system and hence also have a different $\Omega$ but the physical solution always should be the one with the lower $\Omega$.

Figure 2 shows $\Omega$ as a function of temperature for the paramagnetic, AF-I, and AF-II solutions. For the paramagnetic phase to good approximation $\Omega(T) = \Omega_0 - k_B T \ln(3)$ where $k_B \ln(3)$ is the entropy due to the threefold degenerate ${}^3A_{2g}$ ground state of a single $Ni^{2+}$ ion with configuration $t_{2g}^6 e_g^2$. At $T_N$ the solution AF-I branches off as would be expected for a second-order phase transition. At 237.5 K, there is a crossing with finite difference of slopes between the AF-I and the AF-II solutions. This would imply a first-order phase transition which most probably is unphysical. Rather, this may be the way in which the VCA approximates a continuous but rapid change of the electronic state.

We discuss the phase transition at $T_N$. As usual, we introduce the staggered magnetization $m_s$,

$$m_s = -\frac{\partial \Omega}{\partial h_s}, \tag{18}$$

and switch to the Legendre-transformed potential $\Omega'(m_s) = \Omega(h_s) + m_s h_s$ which, using (15), is

$$\Omega'(m_s) = \tfrac{1}{2}\,\mu_B^2\,\chi_s^{-1}\,m_s^2 + O\left(m_s^4\right).$$

In the present situation where the chemical potential is within the sizable insulating gap, this equals the Gibbs free energy up to an additive constant. Comparison with (16) shows that the lowest-order term in the expansion of $\Omega'(m_s)$ has the form expected from Landau theory:

$$\Omega'(m_s) = a(T - T_N)m_s^2 + \frac{b}{2}\,m_s^4$$

with $a = 1/(2C_s)$. To carry this further, we use

$$h_s = \frac{\partial \Omega'}{\partial m_s} = 2a(T - T_N)m_s + 2bm_s^3.$$

The dependence of $h_s$ on $m_s$ can be obtained within the VCA by increasing the staggered field $h_s$ in small steps starting from $h_s = 0$, thereby always using the converged AF-I solution for the preceding step as starting point for the Newton algorithm for the next $h_s$. After convergence, $m_s$ is obtained from (18). The resulting curves are shown in Fig. 3. At 470 K, the magnetization is opposite to the field because below $T_N$ the paramagnetic state and hence also the states "close" to it are unstable and in fact this behavior is precisely what is expected from Landau theory. Namely, $h_s(m_s)$ can be fitted by a third-order polynomial $h_s = c_1 m_s + c_2 m_s^3$ with $c_1 = -0.484\,\text{meV}$, $c_2 = 2.339\,\text{meV}$ at 470 K and $c_1 = 0.322\,\text{meV}$, $c_2 = 2.458\,\text{meV}$ at 490 K. From the rather similar values of $c_2$ we can conclude that $b \approx 1.20\,\text{meV}$. Evaluating $c_1$ from $c_1 = 2a(T - T_N)$ gives $c_1 = -0.447\,\text{meV}$ at 470 K and $c_1 = 0.362\,\text{meV}$ at 490 K, reasonably consistent with the values extracted from $m_s(h_s)$. Figure 4 shows the difference $\Omega_{\text{para}} - \Omega_{\text{AF}}$. Since both are calculated in zero external field we have $\Omega' = \Omega$ and we expect

$$\Omega_{\text{para}}(T) - \Omega_{\text{AF}}(T) = A(T - T_N)^2.$$

The fit gives $A = 1.746 \times 10^{-4}\,\text{meV K}^{-2}$ whereas using $a^2/(2b) = 1.694 \times 10^{-4}\,\text{meV K}^{-2}$. Figure 4 also shows the ordered moment $m_s = \langle n_{d,\uparrow}\rangle - \langle n_{d,\downarrow}\rangle$ versus temperature. Close to $T_N$ this can be fitted by $m_s(T) = B\sqrt{T_N - T}$ with $B = 0.131\,K^{-1/2}$ (for comparison: $\sqrt{(a/b)} = 0.130\,K^{-1/2}$). The symmetry-breaking parameters $V_-(e_g)$ and $\epsilon_{d,-}(e_g)$ have a similar $T$ dependence $\propto\sqrt{T_N - T}$ close to $T_N$. All in all, the phase transition is described well by Landau theory and the VCA allows to extract the parameters of the theory from the original Hamiltonian.

Next, we consider the specific heat $C(T)$ which is shown in Fig. 5. The top panel shows experimental data for NiO taken

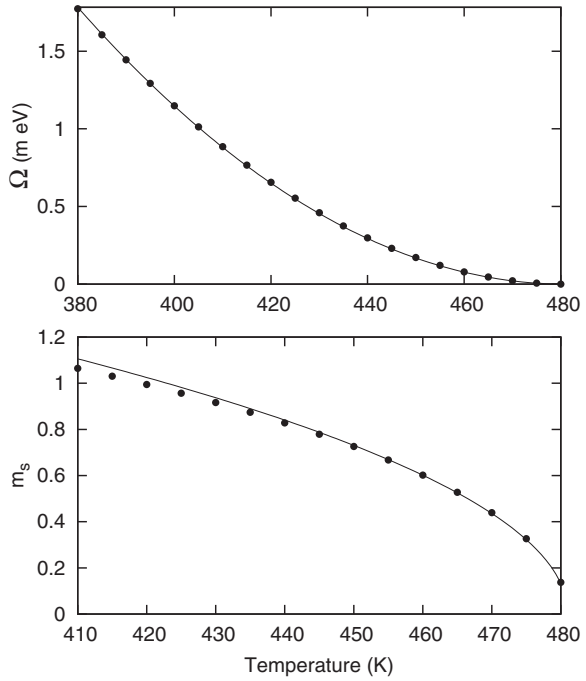


FIG. 4. Top: difference of the grand potential in the paramagnetic phase and in the antiferromagnetic phase versus temperature (dots) and fit (line). Bottom: ordered moment versus temperature (dots) and fit (line).

from Refs. [74–76]. Also shown is the phonon contribution which was calculated from the phonon spectrum measured by inelastic neutron scattering at room temperature [77]. The electronic heat capacity $C_{el}$ is compared to the VCA result in the lower part of the figure. The VCA of course does not reproduce the divergence of $C_{el}$ at the ordering transition which follows the critical exponents for a three-dimensional

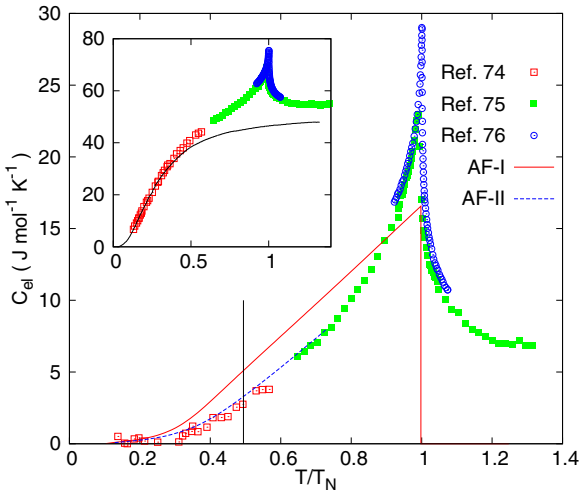


FIG. 5. (Color online) Experimental electronic specific heat as obtained by different authors [74–76] compared to the VCA result. The vertical line gives the temperature where the solutions AF-I and AF-II cross (see Fig. 2). The inset shows the experimental raw data, the line gives the phonon contribution (taken from Ref. [77]) which was subtracted to obtain the electronic contribution.

(3D) Heisenberg antiferromagnet [76]. Apart from that, the result from the VCA is roughly consistent with the measured values, especially the solution AF-II agrees quite well with the data at low temperature. In fact, this solution appears to match the experimental data considerably better up to $\approx 0.7\,T_N$. This may be an indication that in NiO this solution is realized even at temperatures well above the transition between AF-I and AF-II at 237.5 K (which is indicated by the vertical line in Fig. 5). In fact, as will be seen in the following, the single-particle spectral function for this solution matches the experimental photoelectron spectra, which are usually taken at room temperature, quite well.

The apparently large value of $C_{el}$ above $T_N$ probably is an artifact: the phonon spectrum was measured at room temperature that means where the lattice was deformed by magnetostriction. Above $T_N$, this deformation is absent and the phonon spectrum may change so that using the low-temperature phonon spectrum gives an incorrect estimate for the phonon contribution. The electronic heat capacity per mole obeys the sum rule

$$\int_0^{T_h} \frac{C_{el}(T)}{T}\,dT = R\,\ln(3),$$

where $T_h$ is well above the Néel temperature. It turns out that the experimental data exhaust this sum rule at $T_h \approx 660$ K.

Finally, Table I compares the parameter values for the paramagnetic and AF-II solutions at 200 K, as well as various observables. The expectation value of any term $H_{\text{part}}$ in the Hamiltonian can be calculated by replacing $H_{\text{part}} \to \zeta H_{\text{part}}$

TABLE I. Top: parameters of the AF-II (AF) and paramagnetic (Para) solution at 200 K. $\Delta$ = AF-Para. Center part: various contributions to $\Omega$ (energies in eV per Ni). Bottom part: occupation numbers of the Ni $3d$ shell.

| | AF | Para | $\Delta$ |
|---|---|---|---|
| $e_d(e_g)\uparrow$ | −51.4113 | −51.5278 | |
| $e_d(e_g)\downarrow$ | −50.9896 | −51.5278 | |
| $V(e_g)\uparrow$ | −1.4880 | −1.7260 | |
| $V(e_g)\downarrow$ | 0.0000 | −1.7260 | |
| $e_L(e_g)\uparrow$ | 4.3633 | 3.4089 | |
| $e_L(e_g)\downarrow$ | 4.3633 | 3.4089 | |
| $e_d(t_{2g})\uparrow$ | −51.1777 | −51.2256 | |
| $e_d(t_{2g})\downarrow$ | −51.0794 | −51.2256 | |
| $\Omega + \mu N$ | −244.0363 | −244.0235 | −0.0128 |
| $\langle H\rangle$ | −244.0344 | −244.0046 | −0.0299 |
| $S/k_B$ | 0.1090 | 1.0977 | −0.9888 |
| $\langle H_0\rangle$ | −457.9924 | −457.3822 | −0.6102 |
| $\langle H_1\rangle$ | 213.9579 | 213.3776 | 0.5803 |
| $\langle H_{pd}\rangle$ | −3.5283 | −3.4380 | −0.0903 |
| $\langle H_{pp}\rangle$ | −0.1915 | −0.1757 | −0.0158 |
| $\langle H_{dd}\rangle$ | −0.0030 | −0.0034 | 0.0004 |
| $\langle n_{e_g,\uparrow}\rangle$ | 0.2247 | 1.0945 | −0.8698 |
| $\langle n_{e_g,\downarrow}\rangle$ | 1.9738 | 1.0945 | 0.8793 |
| $\langle n_d\rangle$ | 8.1985 | 8.1890 | 0.0095 |
| $\langle n_{t_{2g},\uparrow}\rangle$ | 3.0000 | 3.0000 | 0.0000 |
| $\langle n_{t_{2g},\downarrow}\rangle$ | 3.0000 | 3.0000 | 0.0000 |

and using

$$\langle H_{\rm part}\rangle = \left.\frac{\partial\Omega}{\partial\zeta}\right|_{\zeta=1}.$$

The numerical calculation of the derivative thereby is simplified considerably by taking into account that due to the stationarity condition for the $\lambda_i$ their variation with $\zeta$ can be neglected [57]. The antiferromagnetic unit cell and **k** mesh were used also for the paramagnetic calculation to avoid artifacts.

A somewhat surprising feature is that the quite different cluster parameters for the two different solutions give only slightly different $\Omega$. As expected, $\Omega$ is lower for the antiferromagnetic phase due to the lower energy $\langle H\rangle$. This is partly compensated by the almost complete loss of entropy in the AF phase, but at the low temperature considered this does not result in a higher $\Omega$. As already mentioned, the entropy in the paramagnetic phase is close to $S/k_B = \ln(3) = 1.0986$ as expected for a system of localized $S = 1$ spins. While this may seem trivial, it should be noted that the spin degeneracy can only be reproduced if a spin-rotation-invariant Hamiltonian is used. Discarding the off-diagonal matrix elements of the Coulomb interaction (1) breaks the spin-rotation symmetry so that the entropy of the paramagnetic phase cannot be obtained correctly.

The considerably lower value of $\langle H_0\rangle$ in the AF phase comes about because the $d$ occupancy increases slightly, by 0.0095. With the orbital energy $\epsilon_d = -52$ eV this lowers $\langle H_0\rangle$ by $-0.494$ eV. This is more than compensated, however, by the increase of the Coulomb energy $\langle H_1\rangle$ in the AF phase by 0.5803 eV. Eventually, the energy in the antiferromagnetic phase becomes lower due to the $dp$ hybridization which is lowered by $-0.0903$ eV in the AF phase. Consistent with the theory of superexchange, the driving force behind the antiferromagnetic ordering is not the lowering of the Coulomb energy but a gain of kinetic energy. Interestingly, there is also a significant, on the scale of the change of $\langle H\rangle$, gain in the direct O $2p$–O $2p$ hopping energy $\langle H_{pp}\rangle$ in the AF phase. This is due to the increased charge transfer to Ni $3d$ which reduces the filling of the O $2p$ orbitals and thus allows for enhanced O $2p$–O $2p$ hopping. This contribution is missed in models for superexchange which consider only a single Ni-O-Ni bond.

We summarize the results of the two preceding sections as follows: The description of the magnetic properties and phase transition of NiO as obtained by the VCA is very similar to what would be obtained from a simple mean-field treatment of a localized spin system. It should be noted, however, that the Hamiltonian does not contain any exchange terms nor is there any molecular field in the physical system. Rather, the Hamiltonian is the one for the full NiO lattice (3), the self-energy is calculated in a cluster containing a single Ni ion, and the coupling between Ni ions is solely due to the lattice kinetic energy. Still, the VCA even captures subtle details such as the presence of different exchange channels as manifested by the different values of $T_N$ and $\Theta_{\rm CW}$. It should also be kept in mind that all parameters in the original Hamiltonian are several orders of magnitude larger than the differences in energy in Table I, but still the calculated Néel temperature is quite close to the experimental value (although inclusion of spatial spin correlations which are neglected in the present calculation would probably reduce $T_N$). The VCA thus appears successful in correctly extracting the low-energy scales relevant for ordering phenomena and thermodynamics from the high-energy scales of Hubbard $U$, charge transfer energy, and hopping parameters.

## V. PHOTOELECTRON SPECTRA IN THE ANTIFERROMAGNETIC PHASE

We proceed to a discussion of "high-energy physics" and consider the single-particle spectral function. Figure 6 shows the $\boldsymbol{k}$-integrated spectral density

$$A(\omega) = -\frac{1}{\pi}\sum_{\boldsymbol{k}\alpha} G_{\alpha,\alpha}(\boldsymbol{k},\omega+i\eta), \tag{19}$$

where the sum over $\alpha$ runs over either the Ni $3d$ or the O $2p$ orbitals. The spectral density was calculated for the antiferromagnetic solution AF-II at 200 K. Experiments are usually done at room temperature where according to Fig. 5 the solution AF-I has lower $\Omega$. However, the spectra of the AF-II solution agree better with experiment which might suggest that in reality the crossover between the two solutions occurs already above room temperature; after all, the difference in $\Omega$ between the two solutions is very small. This assumption would also be consistent with the specific-heat data in Fig. 5 where the AF-II solution agrees better with experiment up to

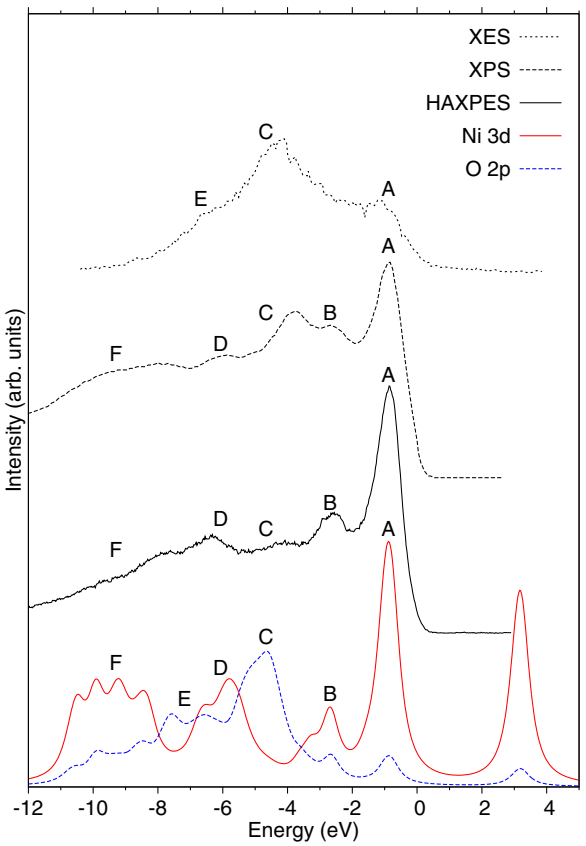


FIG. 6. (Color online) $\boldsymbol{k}$-integrated spectral function $A(\omega)$ for the antiferromagnetic solution AF-II at 200 K compared to experimental spectra.

rather high temperatures. To be consistent, the figure shows the spectra at 200 K where the AF-II solution really does have the lowest Ω. The AF-II solution has a very weak temperature dependence and the spectra at room temperature do not differ appreciably from those at 200 K.

Figure 6 also shows different experimental angle-integrated spectra: First, hard x-ray photoelectron spectroscopy (HAXPES) with a photon energy of $h\nu = 6500$ eV [78]; at this energy the photoionization cross section for Ni $3d$ is approximately 10 times larger than that for O $2p$ so that predominantly the Ni $3d$ density of states is observed. Second, an x-ray photoemission (XPS) spectrum taken with a photon energy of $h\nu = 67$ eV [79]. This is close to the Ni $3p \rightarrow 3d$ absorption threshold so that the satellite region around $-10$ eV is resonantly enhanced [80]. And, third, an x-ray emission (XES) spectrum which shows predominantly the O $2p$ density of states [81].

Several peaks in the theoretical spectra can be identified in the various experimental spectra: these are the peaks $A$ and $B$ which have Ni $3d$ character and thus appear in HAXPES and XPS (although at $h\nu = 67$ eV the peak $A$ is antiresonantly suppressed). The peak $A$ also has some oxygen admixture so that together with peak $C$ it can also be seen in the XES spectrum. Peak $C$ also corresponds to a weak feature observed in HAXPES and in the XPS spectrum. Peak $D$ can be seen both in HAXPES and XPS and the tail of the XES spectrum towards negative energy also shows an indication of the additional shoulder $E$ which corresponds to a similar feature in the theoretical O $2p$ spectrum. Finally, the rather broad feature $F$ can be seen very well in the XPS spectrum. By and large there is good agreement between calculated and measured spectra. It has to be kept in mind, however, that as far as the Ni $3d$ density is concerned, a similar degree of agreement has been obtained earlier by Fujimori and Minami [20] and van Elp *et al.* [26] by the cluster method. The discussion so far shows mainly that as far as angle-integrated spectra are concerned, the VCA "inherits" the accuracy of the cluster method.

We therefore turn to the quantity which allows for the most detailed comparison to experiment, namely, the $\boldsymbol{k}$-resolved spectral density:

$$A(\boldsymbol{k},\omega) = -\frac{1}{\pi}\sum_{\alpha} G_{\alpha,\alpha}(\boldsymbol{k},\omega + i\eta), \tag{20}$$

where the sum over $\alpha$ now runs over both the Ni $3d$ and the O $2p$ orbitals. The dispersion of peaks in $A(\boldsymbol{k},\omega)$ can be compared to the band structure as measured in angle-resolved photoemission spectroscopy (ARPES). To date, there are two ARPES studies of NiO, one by Shen *et al.* [82] and the other by Kuhlenbeck *et al.* [83]. Shen *et al.* give three different sets of data points: the bands from Γ to $X = (\frac{2\pi}{a},0,0)$ [i.e., the (1,0,0) direction] measured in normal and off-normal emission and the bands from Γ to $X_1 = (\frac{2\pi}{a},\frac{2\pi}{a},0)$ [i.e., the (1,1,0) direction)] measured in off-normal emission. The two data sets along $\Gamma - X$ agree for some bands but differ for others due to matrix-element effects. If a given band is observed in any one experimental geometry it obviously does exist, and if it is not observed in another geometry this can only be a matrix-element effect. The true band structure along $\Gamma - X$ thus should comprise at least the superposition of the two sets of

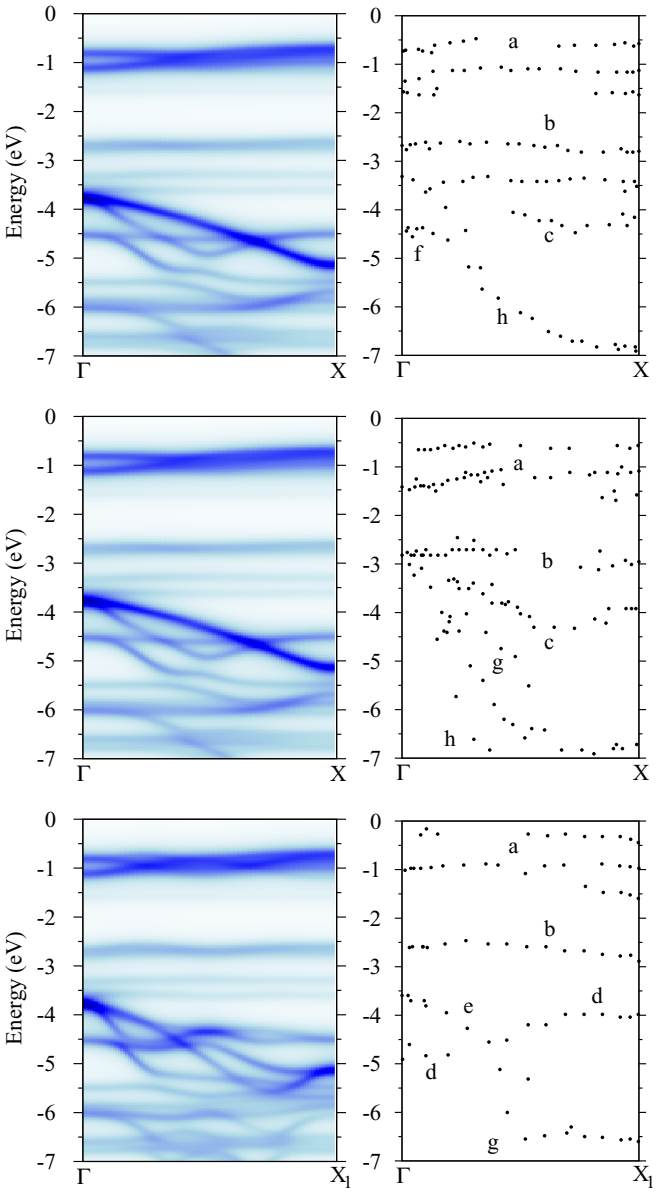


FIG. 7. (Color online) Single-particle spectral density $A(\boldsymbol{k},\omega)$ for the antiferromagnetic solution AF-II at 200 K compared to ARPES data by Shen *et al.* [82]. The three panels show the data for off-normal emission along $\Gamma - X$ (top), normal emission along $\Gamma - X$ (middle), and off-normal emission along $\Gamma - X_1$ (bottom).

bands for normal and off-normal emission. Figure 7 compares $A(\boldsymbol{k},\omega)$ and the respective experimental band dispersions. For both directions, the top of the band structure is formed by a complex of several closely spaced bands with high spectral weight in the range $-0.5 \rightarrow -1.5$ eV, labeled $a$ in the figure. In the angle-integrated spectrum in Fig. 6, these bands produce the intense peak $A$. The high spectral weight of these bands can also be seen in the experimental spectra in Figs. 7 and 8 of Shen *et al.* Below this group of bands there is a gap of approximately 1 eV. In the range $-2.5 \rightarrow -3.5$ eV, there are several essentially dispersionless bands with weak intensity, labeled $b$. In the angle-integrated spectrum in Fig. 6, these bands produce the weak feature $B$. Shen *et al.* resolved two such bands along (1,0,0) but only one along (1,1,0); since the

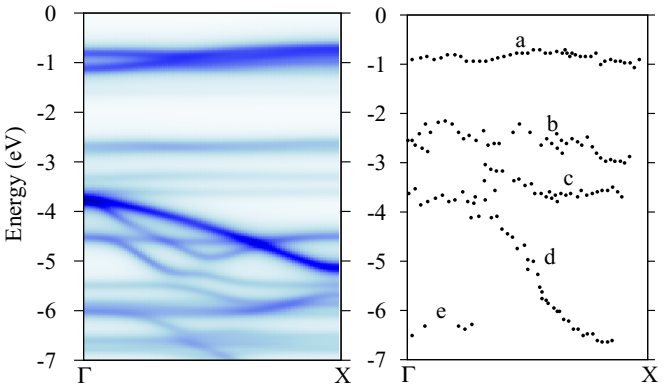


FIG. 8. (Color online) Single-particle spectral density $A(\boldsymbol{k},\omega)$ for the antiferromagnetic solution AF-II at 200 K compared to the ARPES data by Kuhlenbeck *et al.* [83].

dispersions must match at Γ there probably are more than one of these dispersionless bands also along (1,1,0).

Such (nearly) dispersionless bands can be seen also at even more negative energies, but there they are superimposed over and mix with the strongly dispersive O $2p$ derived bands which results in more $\boldsymbol{k}$ dependence. The O $2p$ bands have a stronger dispersion because the respective hopping integrals are larger and because they are taken as uncorrelated. To begin with, there is the dispersive band $c$ along (1,0,0) and $e$ along (1,1,0). In experiment band $c$ shows a relatively strong upward bend near $X$; this may indicate that there rather a part of the dispersionless band which starts at Γ at $\approx -4.6$ eV has been observed. This dispersionless band and its "avoided crossing" with a strongly dispersive O $2p$ derived band $c$ as predicted by the VCA may also have been observed near Γ (see the region labeled $f$ in the top panel of Fig. 7). Along (1,1,0) this dispersionless band can be followed over the full **k** range (see the band labeled $d$ in the bottom panel of Fig. 7). In normal emission (middle panel of Fig. 7) it moreover becomes apparent that the strongly downward dispersing O $2p$ band indeed splits into two bands with opposite curvature (see the region labeled $g$) which would be similar to the VCA bands. Lastly, at $\approx -6.6$ eV another dispersionless band, labeled $g$ and $h$ in the middle and bottom panels of Fig. 7, is observed which would correspond to the nearly dispersionless band which starts out from Γ at slightly below $-6$ eV (and which gives rise to the peak $D$ in the angle-integrated spectrum in Fig. 6).

Some of the above interpretations are corroborated in Fig. 8 which shows a comparison to the band structure deduced by Kuhlenbeck *et al.* along $\Gamma - X$ [83]. There the dispersionless bands $a$, $b$, and $c$ obviously correspond to the bands with the same labels in the data by Shen *et al.*, and the corresponding bands predicted by the VCA. Particularly interesting is the band portion labeled $d$ in Fig. 8 which also shows a peculiar downward curvature and corresponds exactly to the part labeled $g$ in Fig. 7, which in turn had some counterpart in the VCA bands (plotting the two experimental band structures on top of each other shows the exact correspondence of these two bands). Finally, the dispersionless band portion $e$ is precisely the continuation towards Γ of the dispersionless band labeled $h$ in Fig. 7, which also has its counterpart in the VCA band structure.

Generally speaking for all bands which should be easy to observe because they either have a high intensity or are relatively isolated from other bands there is an essentially one-to-one correspondence between VCA and experiment. The VCA predicts a multitude of dispersive low-intensity bands below $\approx -4$ eV and only a few of these seem to have been observed. Combining the three experimental spectra along $\Gamma - X$ indicates, however, that the experimental band structure in this energy range does not consist just of the three strongly dispersive O $2p$ derived bands obtained by band-structure calculations [2] which are also predicted by many "correlated" calculations as well [16,17]. Rather, additional bands, both dispersive and nondispersive, appear to be observed. In the next section, it will be shown that the dispersionless bands are in fact the very fingerprints of the atomic multiplets in the ARPES spectra.

To conclude this section, we discuss the temperature dependence of the spectra. The bottom part of Fig. 9 compares the angle-integrated Ni $3d$ like spectral function for the AF-II solution at 200 K and for the paramagnetic solution at 520 K (the paramagnetic solution has practically no temperature dependence). While the spectra have very similar overall

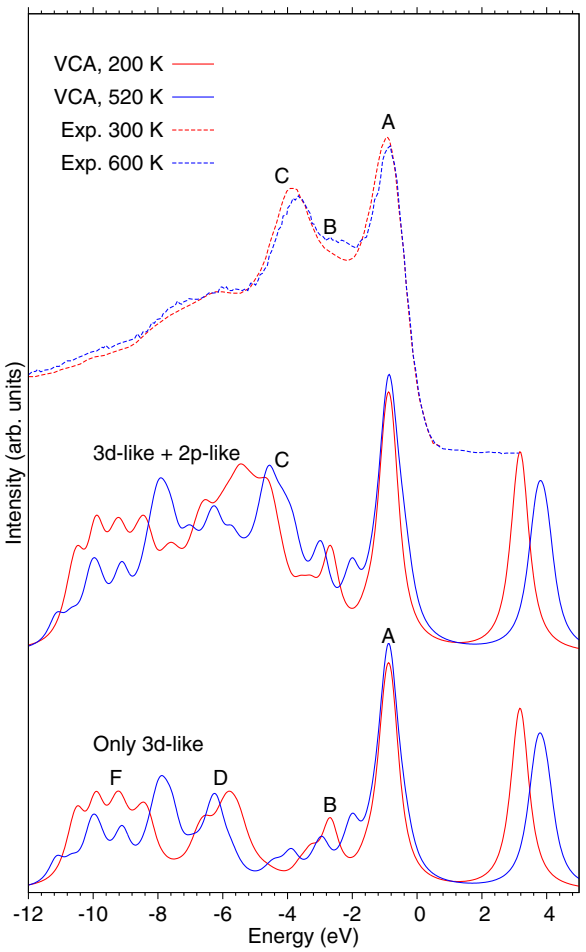


FIG. 9. (Color online) **k**-integrated spectral density for the antiferromagnetic AF-II solution at 200 K and the paramagnetic solution at 520 K. Also shown are experimental spectra by Tjernberg *et al.* measured below and above the experimental Néel temperature of 523 K.

shape, there are small differences. The gap between the large peaks $A$ and $D$ is filled with weight and the relatively well-defined peak $B$ more or less disappears in the paramagnetic phase. A rather strong redistribution of weight occurs in the satellite region were weight disappears between $-11$ and $-8$ eV and a new strong peak grows at $\approx -8$ eV.

Figure 9 also shows the experimental spectrum taken by Tjernberg *et al.* [79] at 615 K, which is well above $T_N$, and a modified version of the spectrum at 300 K. More precisely, the 300-K spectrum was broadened by convolution with a Gaussian to simulate the enhanced thermal broadening and fitted to the high-temperature spectrum whereby both spectra were normalized to unity [79]. Due to the relatively low photon energy $h\nu = 65$ eV, the experimental spectrum also contains a considerable amount of O $2p$ weight, which gives rise to the intense peak $C$ (compare Fig. 6). Accordingly, Fig. 9 also shows the sum of Ni $3d$ like and O $2p$ like spectral functions. In the experimental spectrum, the peak $A$ loses weight in the paramagnetic phase whereas the opposite is predicted by the calculation. In experiment, the spectral weight in the energy range between the two large peaks $A$ and $C$ increases in the paramagnetic phase and a similar change occurs in the theoretical spectra where the relatively well-defined gap between the peaks $A$ and $C$ is partly filled in the paramagnetic spectrum, although the effect seems less pronounced in experiment. In experiment, the peak $C$ loses a small amount of spectral weight and is shifted to slightly less negative energy in the paramagnetic phase. A similar tendency can be seen in the theoretical spectra but considerably exaggerated. Lastly, in experiment the spectral weight increases slightly at various positions in the satellite region below $-8$ eV but no decrease is observed anywhere. In contrast to this in the theoretical spectra there is a drastic change in the satellite region where a considerable amount of weight disappears around $-10$ eV and a new strong peak appears at approximately $-8$ eV. Summarizing, the VCA is only partly successful in predicting the changes of the photoemission spectrum across the Néel temperature. It has to be kept in mind, however, that the photon energy of 65 eV used in the experiment is close to the $3p \rightarrow 3d$ absorption threshold so that the satellite (peak $A$) is resonantly enhanced (antiresonantly suppressed). In fact, the intensities of the various peaks are quite different from the HAXPES spectrum in Fig. 6. Accordingly, additional effects may come into play which determine the intensity of these features and this might be one explanation why discrepancies with theory occur precisely for peak $A$ and the satellite. In any way some of the observed changes with temperature, or actually between antiferromagnetic and paramagnetic phase, appear to be reproduced qualitatively by the VCA. Lastly, Fig. 9 also shows a somewhat surprising difference between the single-particle spectra in the antiferromagnetic and paramagnetic phases, namely, the insulating gap in the paramagnetic phase is larger than in the antiferromagnetic phase. More precisely, the peak-to-peak distances are 4.65 and 4.05 eV so that the gap increases by $\approx$10 %. So far, the temperature dependence of the insulating gap in NiO has not been studied experimentally. As will be discussed in the next section, however, there is a clear physical reason reason for this discrepancy, namely, the fact that the mechanism which opens the insulating gap in the two phases is quite different.

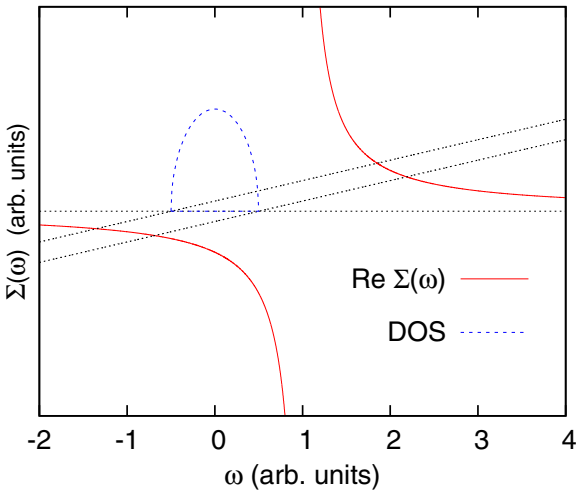


FIG. 10. (Color online) Graphical solution of Eq. (22). The self-energy has a single pole at $\zeta = 1$.

## VI. DISCUSSION OF THE SELF-ENERGY

We discuss some of the results presented in the preceding section from the "self-energy perspective." Luttinger has shown [84] that for a single-band system, the self-energy has a spectral representation of the form

$$\Sigma(\omega) = \eta + \sum_i \frac{\sigma_i}{\omega - \zeta_i}, \tag{21}$$

where $\eta$, $\sigma_i > 0$, and $\zeta_i$ are real. In the following, we assume these parameters to be $\mathbf{k}$ independent. The equation for the poles of the Green's function reads as

$$\omega_k - \epsilon_k = \sum_i \frac{\sigma_i}{\omega_k - \zeta_i}, \tag{22}$$

where for brevity of notation we have replaced $\epsilon_k + \eta - \mu \rightarrow \epsilon_k$. Let us first assume that we have only a single pole with a large weight. Figure 10 shows the resulting $\Sigma(\omega)$ for real $\omega$. Also shown is the noninteracting density of states for the band $\epsilon_k$, the two straight lines correspond to $\omega - \epsilon_-$ and $\omega - \epsilon_+$ where $\epsilon_-$ and $\epsilon_+$ are the bottom and top of the noninteracting band $\epsilon_k$. The intersections of these lines with $\Sigma(\omega)$ give the solutions of Eq. (22) and there is one solution for any $k$ in-between these. A single isolated pole of $\Sigma(\omega)$ thus splits the noninteracting band into the two Hubbard bands and opens a gap in the spectral function. Such an isolated pole with a residuum $\propto N^0$ in the self-energy obviously is the very essence of a Mott insulator; this can also be seen in the self-energy of the two-dimensional Hubbard model [85]. Figure 11 shows the $e_g$-like self-energy for the paramagnetic solution at 520 K and for the antiferromagnetic AF-II solution at 200 K as well as the respective $\mathbf{k}$-integrated $d$-like spectral function $A(\omega)$. For the paramagnetic solution, there is indeed an isolated intense peak of the self-energy, labeled $G$ in the figure, within the insulating gap. In contrast, no such "gap-opening peak" exists in the self-energy for the antiferromagnetic solution. There, the mechanism which opens the gap is the different value of the additive constants $\eta_\uparrow$ and $\eta_\downarrow$ in the spin-dependent self-energy,

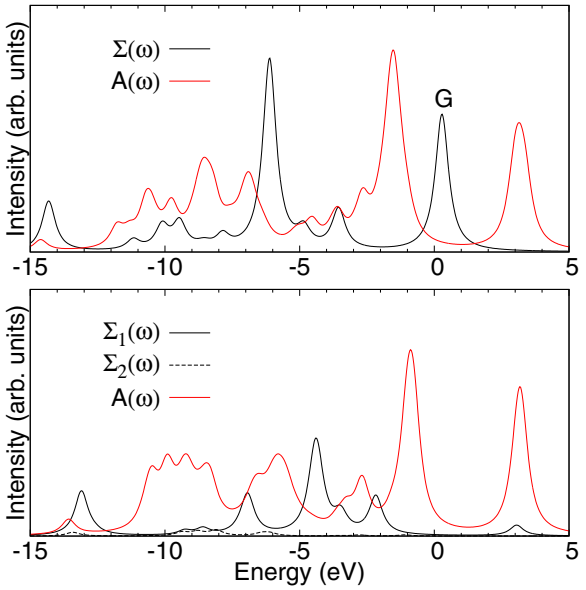


FIG. 11. (Color online) Top: $e_g$-like self-energy $\Sigma(\omega)$ and **k**-integrated $d$-like spectral function $A(\omega)$ for the paramagnetic solution at 520 K. Bottom: same for the AF-II solution at 200 K. The two different self-energies for the antiferromagnetic case refer to the two spin directions. The scale for the self-energy is the same for both panels.

which has the effect of an oscillating potential

$$V_{\mathrm{SDW}}(i) = e^{i\,\boldsymbol{Q}\cdot\boldsymbol{R}_i}\,\frac{\eta_\uparrow - \eta_\downarrow}{2},$$

which opens a gap in the same way as in spin-density-wave mean-field theory. For the AF-II solution at 200 K, $\eta_\uparrow(e_g) = 59.89\,\mathrm{eV}$, $\eta_\downarrow(e_g) = 50.69\,\mathrm{eV}$ [whereby the large average $(\eta_\uparrow + \eta_\downarrow)/2 \approx 55.3\,\mathrm{eV}$ cancels the double-counting correction to the Ni $3d$ level energy]. Since the insulating gaps in the paramagnetic and antiferromagnetic phases are created by different mechanisms, it is not too surprising that they have different values (see Fig. 9). For completeness, we mention that the $t_{2g}$-like self-energy has no such gap-opening peak in either the paramagnetic or insulating phase. This is special for NiO because in the ${}^3A_{2g}$ ground state of $d^8$ in cubic symmetry, which is $t_{2g}^6 e_g^2$, the $t_{2g}$ orbitals are completely filled and thus comprise a "band-insulating" subsystem. Very probably this is also the reason why $V(t_{2g}) = 0$ is a stationary point.

The AF-I solution which branches off the paramagnetic solution at $T_N$ and crosses with the AF-II solution at 237.5 K (see Fig. 2) interpolates between these two types of insulating gap: Figure 12 shows $\Sigma(\omega)$ for this solution for different temperatures. With decreasing temperature, the peak $G$ which opens the insulating gap decreases and shifts to the lower or upper edge of the gap, whereas the value of $\eta_\uparrow - \eta_\downarrow$ increases. NiO thus changes smoothly from a Mott insulator to a spin-density-wave insulator.

Next, we discuss the origin of the dispersionless bands observed in the ARPES spectra of both Shen *et al.* [82] and Kuhlenbeck *et al.* [83]. For the sake of illustration, we consider a model self-energy obtained by arbitrarily choosing a few $\sigma_i$ and $\zeta_i$ in Eq. (21). Figure 13 shows the imaginary part of the resulting $\Sigma(\omega)$ for $\omega$ slightly off the real axis (top) and

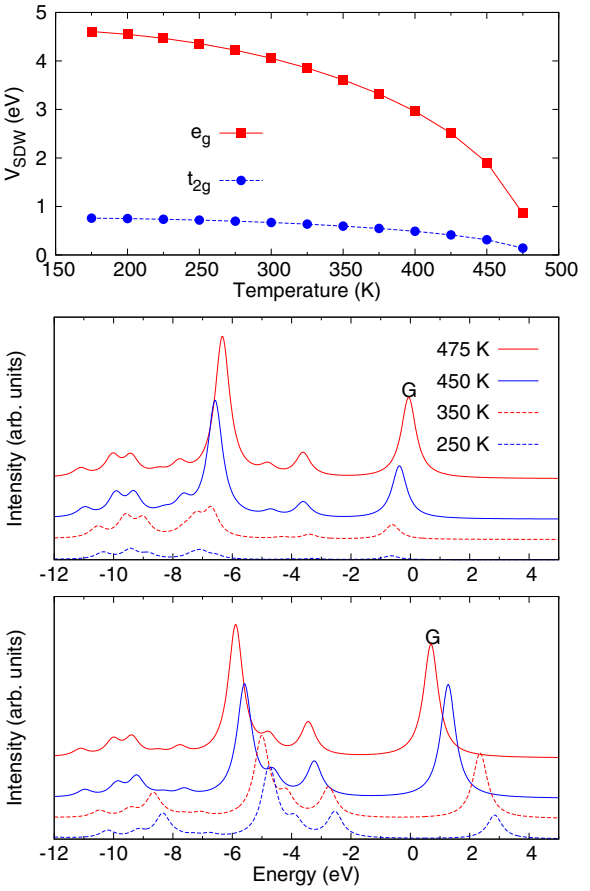


FIG. 12. (Color online) Temperature variation of $V_{\mathrm{SDW}} = (\eta_\uparrow - \eta_\downarrow)/2$ and the $e_g$-like self-energy for the two spin directions in the AF-I solution.

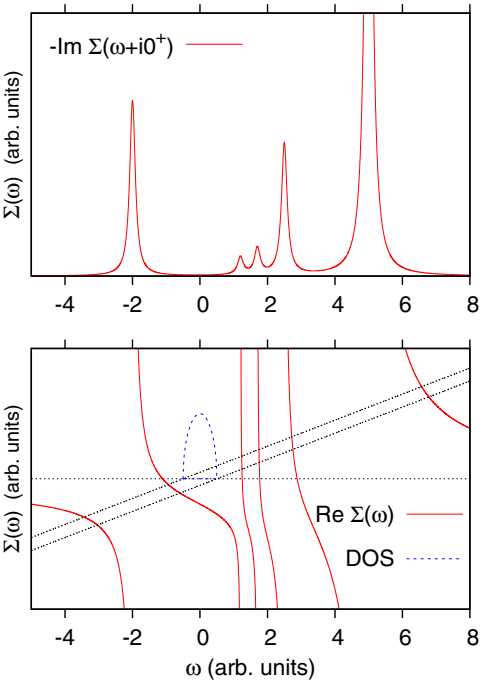


FIG. 13. (Color online) Top: spectral density of the "model self-energy" $\Sigma(\omega)$. Bottom: graphical solution of Eq. (22) for the quasiparticle energies $\omega_k$ with the "model self-energy" $\Sigma(\omega)$.

$\Sigma(\omega)$ for real $\omega$ (bottom). The bottom part again shows the density of states of the noninteracting band $\epsilon_k$ as well as the lines $\omega-\epsilon_-$ and $\omega-\epsilon_+$. For real $\omega$, $\Sigma(\omega)$ takes any value in $[-\infty,\infty]$ precisely once in any interval $[\zeta_i,\zeta_{i+1}]$ so that the line $\omega-\epsilon_k$ intersects $\Sigma(\omega)$ once for each $\epsilon_k$. The point of intersection thereby is between those of the lines $\omega-\epsilon_-$ and $\omega-\epsilon_+$. This shows that in-between any two successive poles of the self-energy there is one complete quasiparticle band. If a given pole has a small $\sigma_i$, however, $\Sigma(\omega)$ drops almost vertically near the corresponding $\zeta_i$, so that the width of the respective band becomes small. Replacing

$$\sum_i \frac{\sigma_i}{\omega-\zeta_i} \to C+\frac{\sigma_0}{\omega-\zeta_0}$$

in the neighborhood of such a pole $\zeta_0$, the resulting dispersion and quasiparticle weight $Z=(1-\frac{\partial\Sigma}{\partial\omega})^{-1}$ are

$$\omega_k \approx \zeta_0+\frac{\sigma_0}{\zeta_0-C-\epsilon_k},$$
$$Z_k \approx \frac{\sigma_0}{(\zeta_0-C-\epsilon_k)^2}.$$

Therefore, unless the denominator happens to cross zero near $\zeta_0$ this results in a band with little dispersion and low spectral weight close to $\zeta_0$. Whether the band is on the high- or low-energy side of $\zeta_0$ depends on the sign of the denominator $\zeta_0-C-\epsilon_k$. Figure 14 compares partial ARPES spectra along (1,0,0), where the sum in Eq. (20) is restricted to either $e_g$-like

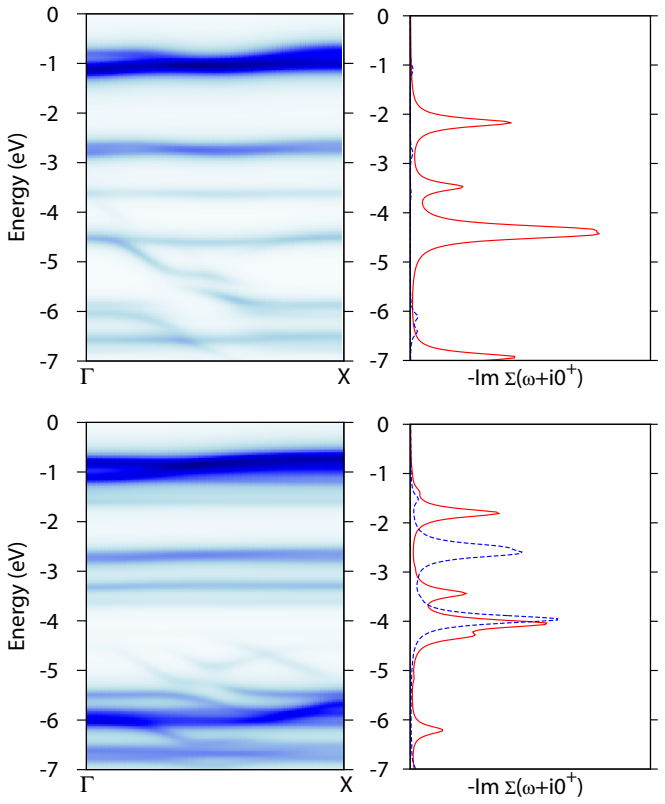


FIG. 14. (Color online) Comparison of partial ARPES spectra and respective self-energy for $e_g$ orbitals (top) and $t_{2g}$ orbitals (bottom). The two different self-energies refer to the two spin directions.

or $t_{2g}$-like Ni $3d$ orbitals and the respective self-energies. Although the situation in NiO is more complicated due to the multiband situation and the hybridization with the O $2p$ bands, it is quite obvious how the various dispersionless bands can be associated with poles of the self-energy. In the case of NiO, these poles describe the multiplet splitting of the final state of the photoemission process, i.e., mainly the $Ni^{3+}$ ion. In the absence of the Coulomb interaction, a single Ni $3d$ shell would have eigenstates obtained by distributing the electrons over the $e_g$ and $t_{2g}$ levels and the single-particle spectral function $A(\omega)$ would have few peaks corresponding to the energies of these crystalline electric field (CEF) levels. The considerably larger number of CEF-split multiplet states in the presence of Coulomb interaction, as given, e.g., in the Tanabe-Sugano diagrams, increases the number of peaks in $A(\omega)$ and the interacting peak structure is generated by the poles of the self-energy of the Ni $3d$ electrons in exactly the same way as in Fig. 13. In the solid, these poles of the self-energy then generate the dispersionless bands observed in ARPES as discussed above. In that sense, one can literally see the dispersionless self-energy of the Ni $3d$ electrons directly in the experimental data of Shen *et al.* and Kuhlenbeck *et al.*

## VII. CONCLUSION

In summary, the variational cluster approximation proposed by Potthoff allows to combine the classic field theoretical work of Luttinger and Ward with the very successful cluster method due to Fujimori and Minami resulting in an efficient band-structure method for strongly correlated electron systems. Since the VCA is based on exact diagonalization which is free from the minus-sign problem, it allows to take into account the full Coulomb interaction in the transition-metal $3d$ shell which is known to be crucial for reproducing the correct multiplet structure and for obtaining agreement with experiment for angle-integrated valence band photoemission [21–29] and x-ray absorption [30–40]. As might have been expected on the basis of the success of the cluster method in describing these spectroscopies, the multiplet structure turns out to be important also for reproducing the experimental valence band structure as observed in ARPES in that it produces a number of nearly dispersionless bands observed there. The VCA moreover delivers an estimate for the grand potential and, as demonstrated above, allows the discussion of thermodynamics and phase transitions. It thereby gives a unified description for a wide variety of experimental quantities which probe energy scales from the meV range up to ≈10 eV.

In the case of NiO, using realistic values of the Hubbard $U$ and charge transfer energy $\Delta$, as demonstrated by the position of the satellite and the magnitude of the insulating gap, and a moderately adjusted value of the Slater-Koster parameter $(pd\sigma)$ (increased by 10% as compared to the LDA band-structure estimate), the theoretical Néel temperature is 481 K (experimental value: 523 K). The behavior near $T_N$ is consistent with a second-order phase transition in a local-moment system, with quite accurate Landau behavior of the free energy and ordered moment below $T_N$ and a Curie-Weiss susceptibility above $T_N$. Consistent with experiment, the angle-integrated density of states is very similar for the paramagnetic and antiferromagnetic phases. The angle-integrated

spectrum and band structure in the antiferromagnetic phase agree well with experiment, whereby the band structure shows a considerable number of both dispersive and dispersionless bands and again shows the massive impact of the strong correlations in NiO in that it differs strongly from the band structure obtained within DFT.

Let us finally briefly return to the issue of the readjustment of the Slater-Koster parameter $(pd\sigma)$ or, more generally, the question of the significance of hopping parameters extracted from LDA band structures. An effect which is usually ignored in calculations for strongly correlated electron systems is the "breathing" of the $3d$ radial wave function with the number of electrons $n$ in the $3d$ shell. This leads to a quite appreciable occupation dependence of Slater integrals and CEF splitting (see, e.g., Ref. [46]) and most likely also to occupation-dependent Slater-Coster parameters. The latter lead to an implicit interaction between Ni $3d$ and O $2p$ electrons which would be very hard to treat. Doing a calculation with occupation-independent Slater-Coster parameters therefore already is an approximation in itself and moreover in an LDA calculation, the Ni $3d$ shell is likely to have an "intermediate" occupation. Bearing this in mind, a readjustment of a parameter by 10% as compared to the LDA estimate appears permissible.


## ACKNOWLEDGMENT

The author would like to thank F. Hardy and K. Grube for help with the specific-heat data and R. Heid for providing the **k** meshes for Brillouin zone integration.


## APPENDIX

In this Appendix, we discuss an unphysical solution which appears when seven parameters are varied. Thereby all four spin-even parameters were varied and in addition to the spin-odd parameters $V_-(e_g)$ and $\epsilon_{e,-}(t_{2g})$ which are used in the AF-I solution, also the spin-odd part of the $e_g$ level energy $\epsilon_{e,-}(e_g)$. The upper part of Fig. 15 shows the temperature dependence of the spin-odd $d$-level-to-ligand hopping $V_-(e_g)$. We could have chosen any other spin-odd parameter, but this one is sufficient to discuss what is happening. The lower part of the figure shows the $\Omega'(T) = \Omega(T) - f(T)$ where $f(T)$ is a second-order polynomial which has no physical significance and was subtracted from $\Omega(T)$ for the sole purpose of making tiny variations of $\Omega$ around this relatively strongly varying but smooth "background" visible.

As one would expect, $V_-(e_g)$ starts to deviate from zero at the Néel temperature $T_N = 481$ K (see point $A$ in the upper part of Fig. 15). At $T_1 \approx 434$ K, a bifurcation occurs and two new solutions appear (see point $B$). At $T_2 \approx 409$ K, another bifurcation occurs and the solution starting out from $A$ disappears (point $C$). The second solution emerging from the bifurcation $C$ can be followed up to temperatures far above $T_N$. As can be seen in the bottom part, the solution along $A \rightarrow C$ has a higher $\Omega$ than the one extending from $C$ to high temperatures (the part above 430 K is omitted for this solution in the bottom part of Fig. 15 to keep the range of $\Omega$ sufficiently small). In fact, $\Omega$ for this solution turns out to be even lower than for the paramagnetic solution so that we have an antiferromagnetic solution which gives the lowest $\Omega$ up to the highest temperatures studied. Moreover, the magnetic solution $A \rightarrow C$ appearing at $T_N$, which would be consistent with the staggered susceptibility, would be an unstable state which never should be realized. One of the two solutions emerging from the bifurcation $B$ intersects the unphysical antiferromagnetic solution at ≈420 K.

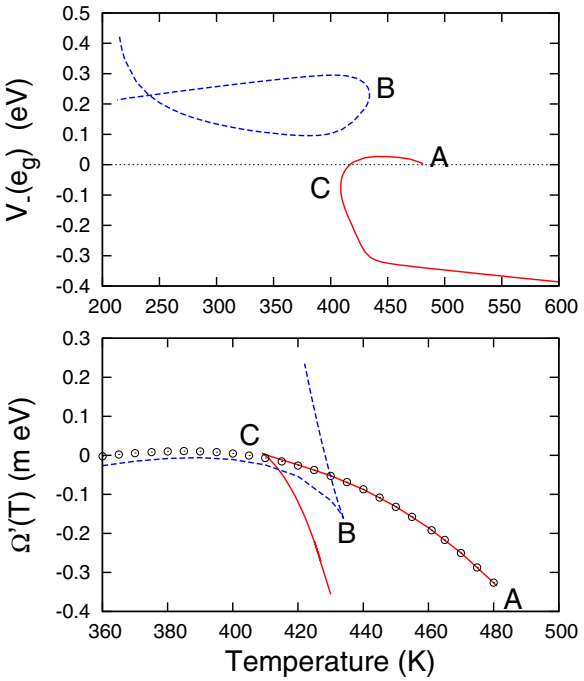


FIG. 15. (Color online) Top: spin-odd hopping parameter $V_-(e_g)$ for the solution with seven parameters as a function of temperature. Bottom: grand potential as a function of temperature for the different solutions with seven parameters (lines). To make small changes visible, the function $f(T) = -2.99067e\times10^{-7}T^2 + 1.06805\times10^{-4}T - 712.08$ was subtracted from $\Omega$. Also shown is $\Omega'(T)$ for the solution AF-I with six parameters (circles).

The bottom part also shows $\Omega'(T)$ for the solution AF-I with six varied parameters. Over almost the entire temperature range this solution is very close in energy (the deviation is $\propto10^{-5}$ eV between 300 and 420 K and even smaller above 440 K) to one of the solutions with seven parameters. In fact, it seems to interpolate between two branches of solutions with seven parameters. That the "closeness" is not restricted to $\Omega$ can be seen in Table II, which compares some physical quantities for the two different solutions, and from Fig. 16, which compares the **k**-integrated spectral densities. Both the table and the figure show an essentially perfect agreement between the two solutions as far as observable quantities are concerned. In contrast to this, the symmetry-breaking parameters $\lambda_{i,-}$ which are also listed in the table are quite different and in fact substantially larger for the solution with seven parameters. This shows that the symmetry-breaking effects of $V_-(e_g)$ and $e_{d,-}(e_g)$ must cancel to a large degree in order to simulate the effect of a significantly smaller $V_-(e_g)$ alone. Adding $e_{d,-}(e_g)$ to the set of parameters to be varied is superfluous. For completeness, we note that keeping $e_{d,-}(t_{2g}) = 0$ so that $V_-(e_g)$ remains as the only spin-odd parameter to be varied gives results which are almost

TABLE II. Left columns: comparison of the AF-I solution with six parameters and the solution for seven parameters at 400 K. Right columns: comparison of the unphysical AF solution and the paramagnetic solution at 600 K. All energies in eV.

| | AF-I | 7 parameters | AF | Para |
|---|---|---|---|---|
| $V_{-}(e_g)$ | 0.0338 | 0.1021 | −0.3865 | 0.0000 |
| $e_{d,-}(e_g)$ | 0.0000 | 0.0414 | −0.2424 | 0.0000 |
| $e_{d,-}(t_{2g})$ | 0.0171 | 0.0198 | −0.0126 | 0.0000 |
| $\Omega + \mu N$ | −244.043562 | −244.043570 | 244.0621 | −244.0613 |
| $\langle H \rangle$ | 244.0169 | 244.0169 | −244.0046 | −244.0045 |
| $S/k_B$ | 0.7734 | 0.7736 | 1.1139 | 1.0981 |
| $\langle H_0 \rangle$ | −457.6312 | −457.6322 | −457.3758 | −457.3815 |
| $\langle H_1 \rangle$ | 213.6143 | 213.6153 | 213.3712 | 213.3770 |
| $\langle H_{pd} \rangle$ | −3.4749 | −3.4750 | −3.4373 | −3.4379 |
| $\langle H_{pp} \rangle$ | −0.1822 | −0.1822 | −0.1756 | −0.1757 |
| $\langle H_{dd} \rangle$ | −0.0032 | −0.0032 | −0.0034 | −0.0034 |
| $\langle n_{e_g,\uparrow} \rangle$ | 0.5325 | 0.5328 | 1.1138 | 1.0945 |
| $\langle n_{e_g,\downarrow} \rangle$ | 1.6604 | 1.6601 | 1.0757 | 1.0945 |
| $\langle n_d \rangle$ | 8.1928 | 8.1929 | 8.1889 | 8.1890 |
| $\langle m_s \rangle$ | −1.1279 | −1.1273 | 0.0376 | 0.0000 |

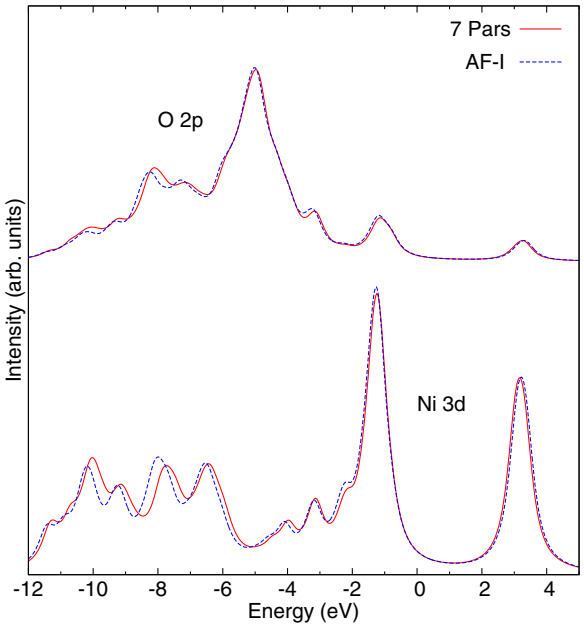


FIG. 16. (Color online) Comparison of the **k**-integrated spectral densities for the AF-I solution with six varied parameters and the solution with seven varied parameters at 400 K.

identical to those for the solution AF-I. From the above it looks very much as if already with six parameters the solution is converged with respect to the number of parameters and that adding an additional spin-odd parameter results in no more significant changes to observables but creates a new branch of unphysical solutions.

We now discuss the artificial antiferromagnetic solution at high temperatures. Table II also compares some observables for this solution and the paramagnetic one at 600 K. As already mentioned, the unphysical solution has lower $\Omega$ than the paramagnetic phase and in addition also a higher entropy. There are no large differences in the various ground-state expectation values. Although the symmetry-breaking parameters $V_{-}(e_g)$ and $e_{d,-}(e_g)$ are substantially larger than those for the antiferromagnetic solutions at 400 K given in Table II, the ordered moment is much smaller. This shows again that the symmetry-breaking effect of the different spin-odd parameters cancels almost completely in this solution.

The above example shows that including too many symmetry-breaking parameters into the subset of variational parameters can lead to unphysical solutions. Here, it is interesting to note that Kozik *et al.* recently reported unphysical solutions obtained by DMFT for the self-energy of a simple Hubbard dimer [86]. A tendency to produce additional unphysical solutions may be a general feature of schemes which aim at computing the self-energy. Within the VCA, the simplest solution to this problem would be to simply restrict the number of parameters to a minimum, as was done in the solution AF-II in the main text. Clearly, this introduces a certain arbitrariness regarding the subset of parameters to be varied. On the other hand, the above discussion shows that results of the VCA appear to converge rather well with the number of variational parameters. In any way, it seems desirable to find criteria which allow to identify unphysical solutions or methods to regularize the variational procedure so that unphysical solutions are suppressed.

[1] J. H. de Boer and E. J. W. Verwey, Proc. Phys. Soc. London **49**, 59 (1937).
[2] L. F. Mattheiss, Phys. Rev. B **5**, 290 (1972).
[3] K. Terakura, T. Oguchi, A. R. Williams, and J. Kubler, Phys. Rev. B **30**, 4734 (1984).
[4] G. A. Sawatzky and J. W. Allen, Phys. Rev. Lett. **53**, 2339 (1984).
[5] M. R. Norman and A. J. Freeman, Phys. Rev. B **33**, 8896(R) (1986).
[6] A. Svane and O. Gunnarsson, Phys. Rev. Lett. **65**, 1148 (1990).
[7] Z. Szotek, W. M. Temmerman, and H. Winter, Phys. Rev. B **47**, 4029(R) (1993).
[8] V. I. Anisimov, I. V. Solovyev, M. A. Korotin, M. T. Czyzyk, and G. A. Sawatzky, Phys. Rev. B **48**, 16929 (1993).
[9] O. Bengone, M. Alouani, P. Blöchl, and J. Hugel, Phys. Rev. B **62**, 16392 (2000).
[10] F. Aryasetiawan and O. Gunnarsson, Phys. Rev. Lett. **74**, 3221 (1995).
[11] S. Massidda, A. Continenza, M. Posternak, and A. Baldereschi, Phys. Rev. B **55**, 13494 (1997).
[12] S. Kobayashi, Y. Nohara, S. Yamamoto, and T. Fujiwara, Phys. Rev. B **78**, 155112 (2008).
[13] F. Manghi, C. Calandra, and S. Ossicini, Phys. Rev. Lett. **73**, 3129 (1994).
[14] M. Takahashi and J. I. Igarashi, Phys. Rev. B **54**, 13566 (1996); Ann. Phys. (NY) **5**, 247 (1996).
[15] J. Kunes, V. I. Anisimov, A. V. Lukoyanov, and D. Vollhardt, Phys. Rev. B **75**, 165115 (2007).

[16] J. Kunes, V. I. Anisimov, S. L. Skornyakov, A. V. Lukoyanov, and D. Vollhardt, Phys. Rev. Lett. **99**, 156404 (2007).
[17] Q. Yin, A. Gordienko, X. Wan, and S. Y. Savrasov, Phys. Rev. Lett. **100**, 066406 (2008).
[18] O. Miura and T. Fujiwara, Phys. Rev. B **77**, 195124 (2008).
[19] R. Gillen and J. Robertson, J. Phys.: Condens. Matter **25**, 165502 (2013).
[20] A. Fujimori and F. Minami, Phys. Rev. B **30**, 957 (1984).
[21] A. Fujimori, M. Saeki, N. Kimizuka, M. Taniguchi, and S. Suga, Phys. Rev. B **34**, 7318 (1986).
[22] J. Ghijsen, L. H. Tjeng, J. van Elp, H. Eskes, J. Westerink, G. A. Sawatzky, and M. T. Czyzyk, Phys. Rev. B **38**, 11322 (1988).
[23] A. Fujimori, N. Kimizuka, T. Akahane, T. Chiba, S. Kimura, F. Minami, K. Siratori, M. Taniguchi, S. Ogawa, and S. Suga, Phys. Rev. B **42**, 7580 (1990).
[24] J. van Elp, R. H. Potze, H. Eskes, R. Berger, and G. A. Sawatzky, Phys. Rev. B **44**, 1530 (1991).
[25] J. van Elp, J. L. Wieland, H. Eskes, P. Kuiper, G. A. Sawatzky, F. M. F. de Groot, and T. S. Turner, Phys. Rev. B **44**, 6090 (1991).
[26] J. van Elp, H. Eskes, P. Kuiper, and G. A. Sawatzky, Phys. Rev. B **45**, 1612 (1992).
[27] M. Abbate, R. Potze, G. A. Sawatzky, and A. Fujimori, Phys. Rev. B **49**, 7210 (1994).
[28] T. Saitoh, T. Mizokawa, A. Fujimori, M. Abbate, Y. Takeda, and M. Takano, Phys. Rev. B **55**, 4257 (1997).
[29] M. Taguchi, M. Matsunami, Y. Ishida, R. Eguchi, A. Chainani, Y. Takata, M. Yabashi, K. Tamasaku, Y. Nishino, T. Ishikawa, Y. Senba, H. Ohashi, and S. Shin, Phys. Rev. Lett. **100**, 206401 (2008).
[30] G. van der Laan, J. Zaanen, G. A. Sawatzky, R. Karnatak, and J.-M. Esteva, Phys. Rev. B **33**, 4253 (1986).
[31] G. van der Laan, B. T. Thole, G. A. Sawatzky, and M. Verdaguer, Phys. Rev. B **37**, 6587(R) (1988).
[32] K. Okada and A. Kotani, J. Phys. Soc. Jpn. **61**, 449 (1992).
[33] A. Tanaka and T. Jo, J. Phys. Soc. Jpn. **61**, 2040 (1992).
[34] F. M. F. de Groot, J. Electron Spectrosc. Relat. Phenom. **67**, 529 (1994).
[35] H. F. Pen, L. H. Tjeng, E. Pellegrin, F. M. F. de Groot, G. A. Sawatzky, M. A. van Veenendaal, and C. T. Chen, Phys. Rev. B **55**, 15500 (1997).
[36] M. Finazzi, N. B. Brookes, and F. M. F. de Groot, Phys. Rev. B **59**, 9933 (1999).
[37] M. W. Haverkort, Z. Hu, J. C. Cezar, T. Burnus, H. Hartmann, M. Reuther, C. Zobel, T. Lorenz, A. Tanaka, N. B. Brookes, H. H. Hsieh, H.-J. Lin, C. T. Chen, and L. H. Tjeng, Phys. Rev. Lett. **97**, 176405 (2006).
[38] M. Merz, D. Fuchs, A. Assmann, S. Uebe, H. V. Löhneysen, P. Nagel, and S. Schuppler, Phys. Rev. B **84**, 014436 (2011).
[39] F. M. F. de Groot, Coord. Chem. Rev. **249**, 31 (2005).
[40] F. M. F. de Groot and A. Kotani, *Core Level Spectroscopy of Solids* (Taylor & Francis, London, 2008).
[41] J. C. Slater, *Quantum Theory of Atomic Structure* (McGraw-Hill, New York, 1960).
[42] J. S. Griffith, *The Theory of Transition-Metal Ions* (Cambridge University Press, Cambridge, UK, 1964).
[43] S. Sugano, Y. Tanabe, and H. Kamimura, *Multiplets of Transition Metal Ions in Crystals* (Academic Press, New York, 1970).
[44] J. Kanamori, Prog. Theor. Phys. **30**, 275 (1963).
[45] D. van der Marel and G. A. Sawatzky, Phys. Rev. B **37**, 10674 (1988).
[46] M. W. Haverkort, Ph.D. thesis, University of Cologne, 2005; see also arXiv:cond-mat/0505214.
[47] E. Gull, A. J. Millis, A. I. Lichtenstein, A. N. Rubtsov, M. Troyer, and P. Werner, Rev. Mod. Phys. **83**, 349 (2011).
[48] M. Potthoff, Eur. Phys. J. B **32**, 429 (2003).
[49] M. Potthoff, Eur. Phys. J. B **36**, 335 (2003).
[50] M. Potthoff, M. Aichhorn, and C. Dahnken, Phys. Rev. Lett. **91**, 206402 (2003).
[51] R. Eder, Phys. Rev. B **78**, 115111 (2008).
[52] J. M. Luttinger and J. C. Ward, Phys. Rev. **118**, 1417 (1960).
[53] M. Potthoff, Condens. Matter Phys. **9**, 557 (2006).
[54] M. Potthoff, in *Theoretical Methods for Strongly Correlated Systems*, edited by A. Avella and F. Mancini (Springer, Berlin, 2011); see also arXiv:1108.2183.
[55] C. Dahnken, M. Aichhorn, W. Hanke, E. Arrigoni, and M. Potthoff, Phys. Rev. B **70**, 245110 (2004).
[56] D. Sénéchal, P.-L. Lavertu, M.-A. Marois, and A.-M. S. Tremblay, Phys. Rev. Lett. **94**, 156404 (2005).
[57] M. Aichhorn, E. Arrigoni, M. Potthoff, and W. Hanke, Phys. Rev. B **74**, 235117 (2006).
[58] A. H. Nevidomskyy, C. Scheiber, D. Sénéchal, and A.-M. S. Tremblay, Phys. Rev. B **77**, 064427 (2008).
[59] M. Balzer, B. Kyung, D. Sénéchal, A.-M. S. Tremblay, and M. Potthoff, Europhys. Lett. **85**, 17002 (2009).
[60] M. Balzer and M. Potthoff, Phys. Rev. B **82**, 174441 (2010).
[61] K. Seki, R. Eder, and Y. Ohta, Phys. Rev. B **84**, 245106 (2011).
[62] A. Yamada, K. Seki, R. Eder, and Y. Ohta, Phys. Rev. B **88**, 075114 (2013).
[63] A. Yamada, Phys. Rev. B **89**, 195108 (2014).
[64] A. Yamada, Phys. Rev. B **90**, 235138 (2014).
[65] A. Yamada, Phys. Rev. B **90**, 245139 (2014).
[66] L. Chioncel, H. Allmaier, E. Arrigoni, A. Yamasaki, M. Daghofer, M. I. Katsnelson, and A. I. Lichtenstein, Phys. Rev. B **75**, 140406 (2007).
[67] H. Allmaier, L. Chioncel, and E. Arrigoni, Phys. Rev. B **79**, 235126 (2009).
[68] M. Aichhorn, T. Saha-Dasgupta, R. Valenti, S. Glawion, M. Sing, and R. Claessen, Phys. Rev. B **80**, 115129 (2009).
[69] R. Eder, Phys. Rev. B **81**, 035101 (2010).
[70] H. Allmaier, L. Chioncel, E. Arrigoni, M. I. Katsnelson, and A. I. Lichtenstein, Phys. Rev. B **81**, 054422 (2010).
[71] W. Koller and N. Dupuis, J. Phys.: Condens. Matter **18**, 9525 (2005).
[72] M. Knap, E. Arrigoni, and W. von der Linden, Phys. Rev. B **81**, 235122 (2010).
[73] J. R. Singer, Phys. Rev. **104**, 929 (1956).
[74] H. Seltz, B. J. DeWitt, and H. J. McDonald, Am. Chem. Soc. **62**, 88 (1940).
[75] B. S. Hemingway, Am. Mineral. **75**, 781 (1990).
[76] M. Massot, A. Oleaga, A. Salazar, D. Prabhakaran, M. Martin, P. Berthet, and G. Dhalenne, Phys. Rev. B **77**, 134438 (2008).
[77] R. A. Coy, C. W. Thompson, and E. Gürmen, Solid State Commun. **18**, 845 (1976).
[78] T. Haupricht, J. Weinen, A. Tanaka, R. Gierth, S. G. Altendorf, Y.-Y. Chin, T. Willers, J. Gegner, H. Fujiwara, F. Strigari, A. Hendricks, D. Regesch, Z. Hu, Hua Wu, K.-D. Tsuei, Y. F. Liao, H. H. Hsieh, H.-J. Lin, C. T. Chen, and L. H. Tjeng, arXiv:1210.6675.

[79] O. Tjernberg, S. Söderholm, G. Chiaia, R. Girard, U. O. Karlsson, H. Nylén, and I. Lindau, Phys. Rev. B **54**, 10245 (1996).
[80] S.-J. Oh, J. W. Allen, I. Lindau, and J. C. Mikkelsen Jr., Phys. Rev. B **26**, 4845 (1982).
[81] E. Z. Kurmaev, R. G. Wilks, A. Moewes, L. D. Finkelstein, S. N. Shamin, and J. Kunes, Phys. Rev. B **77**, 165127 (2008).
[82] Z. X. Shen, R. S. List, D. S. Dessau, B. O. Wells, O. Jepsen, A. J. Arko, R. Barttlet, C. K. Shih, F. Parmigiani, J. C. Huang, and P. A. P. Lindberg, Phys. Rev. B **44**, 3604 (1991).
[83] H. Kuhlenbeck, G. Odörfer, R. Jaeger, G. Illing, M. Menges, Th. Mull, H.-J. Freund, M. Pöhlchen, V. Staemmler, S. Witzel, C. Scharfschwerdt, K. Wennemann, T. Liedtke, and M. Neumann, Phys. Rev. B **43**, 1969 (1991).
[84] J. M. Luttinger, Phys. Rev. **121**, 942 (1961).
[85] R. Eder, K. Seki, and Y. Ohta, Phys. Rev. B **83**, 205137 (2011).
[86] E. Kozik, M. Ferrero, and A. Georges, Phys. Rev. Lett. **114**, 156402 (2015).